HHS Public Access

Author manuscript

Magn Reson Med. Author manuscript; available in PMC 2019 February 07.

Published in final edited form as:

Magn Reson Med. 2014 February ; 71(2): 486–505. doi:10.1002/mrm.24729.

Probing Lung Microstructure with Hyperpolarized Noble Gas Diffusion MRI: Theoretical Models and Experimental Results

Dmitriy A. Yablonskiy[1,*], **Alexander L. Sukstanskii**[1], **James D. Quirk**[1], **Jason C. Woods**[1], and **Mark S. Conradi**[2]

[1]Department of Radiology, Washington University, St. Louis, Missouri, USA

[2]Department of Physics, Washington University, St. Louis, Missouri, USA

Abstract

The introduction of hyperpolarized gases (^{3}He and ^{129}Xe) has opened the door to applications for which gaseous agents are uniquely suited–lung MRI. One of the pulmonary applications, diffusion MRI, relies on measuring Brownian motion of inhaled hyperpolarized gas atoms diffusing in lung airspaces. In this article we provide an overview of the theoretical ideas behind hyperpolarized gas diffusion MRI and the results obtained over the decade-long research. We describe a simple technique based on measuring gas apparent diffusion coefficient (ADC) and an advanced technique, in vivo lung morphometry, that quantifies lung microstructure both in terms of Weibel parameters (acinar airways radii and alveolar depth) and standard metrics (mean linear intercept, surface-to-volume ratio, and alveolar density) that are widely used by lung researchers but were previously available only from invasive lung biopsy. This technique has the ability to provide unique three-dimensional tomographic information on lung microstructure from a less than 15 s MRI scan with results that are in good agreement with direct histological measurements. These safe and sensitive diffusion measurements improve our understanding of lung structure and functioning in health and disease, providing a platform for monitoring the efficacy of therapeutic interventions in clinical trials.

Keywords

MRI; lung morphometry; hyperpolarized gas; diffusion MRI; lung alveoli

Approximately 12 million Americans suffer from chronic obstructive pulmonary diseases (COPD) including chronic bronchitis and emphysema as well as asthma. It is the fourth leading cause of chronic morbidity and mortality in the United States, and is projected to rank fifth in 2020 in burden of disease caused worldwide, according to a study published by the World Bank/World Health Organization (1). Numerous diagnostic tools have been developed to evaluate the presence and the stage of these diseases. The traditional classification for the severity of COPD is based on measurements of airflow limitation during forced expiration (1). Each stage is characterized by the volume of air that can be

*Correspondence to: Dmitriy A. Yablonskiy, Ph.D., Mallinckrodt Institute of Radiology, 4525 Scott Ave., Room 3216, St. Louis, MO 63110. YablonskiyD@wustl.edu or http://bmr.wustl.edu/~dmitriy/.

Additional Supporting Information may be found in the online version of this article.

forcibly exhaled in 1 s (FEV_1) and by the ratio of FEV_1 to the forced vital capacity (FVC). Abnormalities in these tests reflect both the reduction in the force available to drive air out of the lung as a result of emphysematous lung destruction (2) and obstruction to airflow in the smaller conducting airways (3–5). However, the specific pathophysiologic role and contribution of emphysema and small airways abnormalities in expiratory airflow obstruction in COPD has been under debate (6,7). While the role of pathologic changes in small airways has received much attention in recent years (8–10), the early-emphysema component of COPD has not. Conventional pulmonary function tests are insensitive to the onset and initial stages of emphysema (11); the same is valid for conventional chest radiography (12); X-ray CT has substantially greater value for evaluation of emphysema (13); there, enlargement of airspaces and destruction of alveolar walls reduces X-ray attenuation and allows the detection of emphysema, especially in advanced stages (14,15). Studies have shown good correlation between the amount of emphysema determined by this method and the amount measured in pathology specimens (15–17) though smoking-related inflammation and lung remodeling can also alter CT attenuation (18–20).

The major function of the lung, of course, is delivery of oxygen to the body and removing CO_2 from it. The efficiency of oxygen delivery through the lung airspaces to the blood vessel network occupying alveolar walls depends mostly on the structure, integrity, and functioning of pulmonary acinar airways. The morphometry of the pulmonary acinus has been studied in numerous publications (e.g. (10,17,21–30)). These studies provided invaluable information on lung microstructure that is the basis of the current knowledge on lung structure and function. Such geometrical parameters as mean linear intercept (or mean chord length), L_m, lung parenchyma surface-to-volume ratio, S/V, and number of alveoli per unit lung volume, N_v, are most commonly used to characterize lung morphometry (see definitions of these parameters in “An official research policy statement of the ATS” (31)). Although lung stereology has been in use for more than a half century and is considered a gold standard (see recent overviews (32,33)), intense debates about its accuracy in estimating lung morphometry continue (34–41). This is mostly due to the objective problems of lung specimen preparation and the subjective bias in selection of “random” regions of lung parenchyma. The problem is so important that the American Thoracic Society and European Respiratory Society have commissioned a Joint Task Force to define the “Standards for Quantitative Assessment of Lung Structure” (31). However, the clinical and even research utility of “standard” lung morphometry is limited by its invasive nature.

The rapid development during the past two decades of hyperpolarized ^3He and ^{129}Xe gas MR imaging of lung air spaces has resulted from combined advances in the spin physics of optical pumping, affordable high-power diode laser arrays, and MRI strategies for optimum use of the non-renewable spin magnetization. MR imaging with hyperpolarized gas requires the MRI scanner to be equipped with broadband RF amplifiers and specially designed RF coils to transmit and receive signals at the ^3He and ^{129}Xe frequencies and equipment to hyperpolarize ^3He and ^{129}Xe gases. Even though these gases have three orders of magnitude smaller nuclear spin density (at standard pressure) compared with water, by using special laser equipment, they can be hyperpolarized to achieve a polarization almost five orders of magnitude more than the polarization of water protons at room temperature (42–46). This increase in polarization compensates for the decreased density of the gas although it also

places some limitations on the MRI acquisition scheme. As a result, very intense MRI signals, compared with those of water, can be achieved from hyperpolarized ^{3}He and ^{129}Xe gases. This has opened the door to applications for which gaseous agents are uniquely suited, such as lung imaging. The MRI measurements with ^{3}He and ^{129}Xe gases are safe and well-tolerated (47,48) and can be repeated in vivo on a regular basis to serve as a tool for research, clinical, and drug development studies.

The first use of the technology was to produce ventilation images which display the distribution of a single bolus of inhaled ^{3}He gas at breath-hold. For example, high spatial resolution ^{3}He-gas imaging in animals has yielded anatomical images showing many levels of airway branching (49–51); anatomical images of human lungs have been reported from healthy subjects (52) and patients with several types of lung pathology (53). Subsequently, dynamic ^{3}He MRI was used to show the time evolution of gas distribution, with sub-second time resolution (e.g. (54,55)). A quantitative method for measurement of the local fractional ventilation (the fraction of gas replaced with each breath) has also appeared (56). The local oxygen concentration and its decrease during breath-hold have been determined (57,58) from the ^{3}He T_1, allowing the local ventilation–perfusion ratio to be calculated (59). ^{129}Xe gas exchange processes between gas and tissue-dissolved phases have also been studied (60–64). Various improvements and new techniques of hyperpolarized gas MRI in lung imaging have been developed over the years (see, for example, review articles (65–81) and references therein).

Our review is focused on one specific pulmonary application in hyperpolarized gas imaging —diffusion MRI.

DIFFUSION LUNG IMAGING (BACKGROUND)

Diffusion MRI with hyperpolarized gases is based on measurements of hyperpolarized gas diffusion introduced in the lung airspaces during inhalation. Initial applications have focused on studying ^{3}He gas and subsequently progressed to ^{129}Xe. We will discuss ^{3}He first.

In any fluid medium, the atoms or molecules diffuse; that is, the atoms perform a Brownian-motion random walk. In time interval Δ (diffusion time), in the absence of restricting walls or barriers the molecules will move a root mean-square distance $L_1 = (2D_0\Delta)^{1/2}$ along any axis. The parameter D_0 is termed the free diffusion coefficient, which for highly diluted ^{3}He in air at 37°C is about 0.88cm^2/s. Hence ^{3}He gas atoms can wander distances on the order of 1 mm in times as short as 1 ms. The alveolar walls as well as the walls of bronchioles, alveolar ducts, sacs and other branches of the airway tree serve as obstacles to the path of diffusing ^{3}He atoms and limit their displacement. Indeed, for diffusion times around 2 ms, the MR-measured average ^{3}He apparent diffusion coefficient (ADC) in healthy human lungs is approximately 0.20 cm^2/s, more than a factor of four smaller than D_0 (82–84). For short diffusion times (a few milliseconds) the ^{3}He gas can explore mostly alveoli and individual acinar airways and thus is primarily reporting on only those structures. This millisecond diffusion time range is used in most hyperpolarized ^{3}He gas studies (see, e.g. (8,74,78,79,82–111)).

The simplest MR measurement of diffusion is the Stejskal-Tanner-type pulsed field gradient (PFG) experiment (112) in which a free-induction decay MR signal is acted upon by two opposite-polarity gradient pulses (Fig. 1)—the so-called diffusion-sensitizing gradients. This method is restricted by MRI signal T2* decay (on the order of 15–30 ms for ^{3}He and 20–50 ms for ^{129}Xe (113,114)) and can only be used to study short range diffusion. Measurements of the ^{3}He diffusion coefficient at longer diffusion times (seconds) proposed by Owers-Bradley et al. (115) (see also (116–120)) allow exploring the “connectivity” of acinar airways and alveoli thus providing information on airway and alveolar wall integrity (i.e., holes through the walls) and collateral ventilation pathways (118,119). This approach will be discussed later in this review.

In the presence of gradient pulses, nuclear spins suffer a net phase shift proportional to their displacement during the diffusion time Δ, resulting in decreased signal amplitude. In the case of unrestricted diffusion, the MR signal S decays as $S = S_0\exp(-bD_0)$. Here, S_0 is the MR signal intensity in the absence of diffusion-sensitizing gradients, and the b-value is determined by the gradient waveform shape. For the gradient pulses in Figure 1, the corresponding b-value is (84,121):

$$b = (\gamma G_m)^2\left[\delta^2\left(\Delta - \frac{\delta}{3}\right) + \tau\left(\delta^2 - 2\Delta\ \delta + \Delta\ \tau - \frac{7}{6}\delta\ \tau + \frac{8}{15}\tau^2\right)\right] \quad [1]$$

In the presence of barriers such as alveolar walls and walls of lung airways, the diffusive motion is restricted and the MR signal decay is often described in terms of the ADC:

$$S = S_0\exp(-b\cdot \mathrm{ADC}) \quad [2]$$

Contrary to the free diffusion case where ADC is equal to D_0 and depends only on the molecular diffusion properties, the ADC for restricted diffusion evaluated from Eq. [2] depends also on the tissue structure and on the timing details of the gradient waveform and gradient strength.

ADC MEASUREMENTS IN HEALTHY AND EMPHYSEMATOUS LUNGS

ADC measurements are usually done with two b-values thus allowing coverage of a substantial part of the lungs in a single breath-hold. Already initial publications (82–84,87) demonstrated that the ADC of hyperpolarized ^{3}He gas in the lungs dramatically increases in emphysema (compared with normal lungs), suggesting a large potential as a diagnostic tool for clinical applications. Figure 2 shows examples of ventilation images (MRI-measured distribution of ^{3}He gas inhaled by a subject) and ^{3}He gas ADC maps of normal human lungs and lungs with severe emphysema.

The remarkable differences in the ADC values between healthy (0.17 cm^2/s) and diseased (0.52 cm^2/s) lung indicate that diffusion imaging of the lung with hyperpolarized helium could provide a very sensitive tool for clinical evaluation of emphysema. Indeed, Figure 3 demonstrates the correlation between ADC and (a) mean alveolar internal area (AIA) in rats

with elastase induced emphysema (90); (b) mean chord length (MCL) in elastase-induced emphysematous rabbit lungs (102); (c) mean linear intercept (L_m) in healthy and emphysematous human lungs with data obtained at different diffusion times (123); (d) mean linear intercept (L_m) in healthy human lungs and lungs with severe emphysema (124).

In addition to correlation with histology seen in Figure 3, ADC in healthy subjects showed correlation with lung inflation level (125) and subjects' age (96,98,125) (see Fig. 4).

Salerno et al. (83) studied correlations between ^{3}He ADC and spirometric indices (Fig. 5). ADC images were homogeneous in volunteers, but demonstrated regional variations in emphysema patients. The mean and SD of the ADCs for patients were significantly larger than those for volunteers. The mean ADCs for all subjects correlated with the percentage of predicted FEV1 and the ratio FEV1/FVC. Correlations between mean ADC values and pulmonary function test were also reported by Fain et al. (126).

Although Figure 3 shows rather good correlations between ADC and morphometry, several important issues need to be clarified. Even in healthy human lungs ADC exhibits rather broad variability, with different studies (82,88,95,97–99,123,127) reporting results between 0.15 cm^2/s and 0.25 cm^2/s. This is due to the fact that ADC depends not only on lung microstructure but on pulse sequence parameters (diffusion time Δ, *b*-value). Besides, even for fixed pulse sequence parameters, there is no one-to-one correspondence between ADC and lung morphometric parameters (see below Fig. 14). That is why ADC, though quite sensitive and useful, cannot characterize lung microstructure in standard morphometric terms.

Most of the studies above were based on ^{3}He gas measurements. Quite a few authors have also reported measurements of ^{129}Xe-based ADC in healthy and emphysematous lungs (48,102,128–132). Kirby et al. (131) demonstrated a significant correlation between ^{3}He ADC and ^{129}Xe ADC as well as between ADCs and CT measurements. In healthy lungs, ^{3}He ADC and ^{129}Xe ADC were found to be ~0.20 cm^2/s and ~0.055 cm^2/s, respectively; in lungs with COPD, the corresponding values are ~0.55 to 0.6 cm^2/s and 0.07 to 0.09 cm^2/s. In Ref. 130, the mean ^{129}Xe ADC in healthy volunteers was reported ~0.04 cm^2/s. Such a difference in ^{129}Xe ADC could be explained by different experimental conditions, including concentration of ^{129}Xe in gas mixtures. The substantially smaller ADC values for ^{129}Xe as compared with ^{3}He are explained by the considerably smaller free diffusion coefficient of ^{129}Xe versus ^{3}He (see detailed discussion in Theory of Gas Anisotropic Diffusion in Acinar Airways as a Background for Lung Morphometry Technique section).

ADC MEASUREMENTS-OTHER PULMONARY APPLICATIONS

Diffusion MRI with hyperpolarized gases in non-COPD pulmonary diseases has lagged significantly behind, in part because there is no clear biophysical model for what the diffusion changes mean. For example, asthma, which is the second most commonly studied pulmonary disorder using MRI, has primarily been studied using ventilation imaging. Asthma is considered an airways disease and therefore the effect on the alveolar space is uncertain. Further, as the airways disease manifests as ventilation defects in the airways

distal to the flow restriction or obstruction, this lack of signal in the most affected regions precludes diffusion quantitation. Reports of diffusion values in these populations indicate normal values for the ^{3}He or ^{129}Xe ADC and are limited in number, presumably because of the lack of a significant finding. Fain et al. (133) studied 21 asthmatics versus 24 never smokers and 16 COPD and found that the asthma group had slightly lower ADC values. However, since these subjects were also younger than the other groups, which would also decrease ADC, the differences were no longer significant after accounting for age. The age-normalized ADC in asthmatics correlated with FEV1 (% predicted) but not FEV1/FVC.

Wang et al. (120) compared the short and long range ^{3}He ADC in asthmatics, COPD, and healthy subjects. While there was no statistical difference between the asthmatics and age-matched healthy controls, there was a trend toward elevated ADC values in the asthmatics, with a larger effect in the long-range ADC. Since the regions of elevated ADC were focal, the authors hypothesized that the elevated ADC was the result of chronic air trapping due to small airways disease. A mouse model of allergic-sensitization studied by Emami et al. (134) also showed no difference in ADC compared with controls, though there was more population variation in the ADC of the asthmatic mice compared with controls.

Diffusion gas MRI has also found a limited application in studying bronchiolitis obliterans in post-transplantation lungs. Bink et al. (135) reported that in this population, the ^{3}He ADC of healthy transplanted lungs was elevated compared with controls and was further increased in transplanted lungs undergoing chronic rejection. While the increased ADC of the healthy transplanted lungs in this study may be age related (96) (the age of the lung donors was unknown), there is a suggestion that the diffusion coefficient is sensitive to the pulmonary changes post-transplantation.

In humans with pulmonary fibrosis, an elevated ^{3}He ADC was detected by Bink et al. (135), suggesting a dilation of peripheral air spaces. However, a study of the rat bleomycin fibrosis model by Stephen et al. (136) detected a decrease in ADC along with lower variability across the lung, though there was no correlation between ADC and PFT. While these results seem contradictory, they are presumably due to differences between clinical pulmonary fibrosis and the mouse bleomycin model.

In addition to COPD, lung cancer is another major complication of smoking. Mathew et al. (137), using hyperpolarized ^{3}He MRI, examined fifteen patients with lung cancer (in one lung) before radiation therapy. While there were increased ventilation defects in the lung with cancer, there was no difference in ADC between the ipsi-lateral and contralateral lungs, suggesting that there were no changes in lung microstructure beyond the border of the cancerous tissue.

Treatments for cancer also have the potential to change the pulmonary microstructure. Mathew et al. (138) found no statistical difference in ^{3}He ADC between the irradiated and contralateral lung in subjects with radiation-induced lung injury; however, there was a trend toward lower ADC in the contralateral lung. After six months, the contralateral lung showed an increase in ADC and received an increased percentage of the helium dose on ventilation image, whereas no change was observed in the ADC of the irradiated lung. In contrast, Ward

et al. (139) had measured decreased ^{3}He ADC in the irradiated lung of a rat, which was associated with fibrosis. It was suggested that the regions of heavy fibrosis in the clinical study could be masked by ventilation defects (138). A more recent small study by Hegarty et al. (140) measuring anisotropy of ^{129}Xe diffusion in a rat model of radiation induced lung injury found decreased D_T in the irradiated rat lungs and a trend towards decreased D_L (see definitions below).

Recently Narayanan et al. (141) and Cadman et al. (142) have demonstrated pediatric applications in lung microstructure measurements using a q-space technique (143) In particular, the results in Ref. 142 demonstrate a higher degree of restriction to gas diffusion in children with asthma compared with those seen in children without asthma.

THEORETICAL MODELS OF GAS DIFFUSION IN LUNG AIRWAYS

To advance diffusion measurements to research and clinical practice, a fundamental question —what aspects of lung microstructure are being measured by ^{3}He or ^{129}Xe ADC—needs to be answered. To obtain quantitative information on lung microstructure at the acinar level, geometrical parameters describing the lung microstructure should be related to the parameters extracted from MR measurements independent of pulse sequence parameters and/or gas concentration. Obviously, such a complicated structure as lung cannot be analyzed without some simplifications and assumptions. To date numerous models for lung microstructure have been explored to simulate diffusion attenuated MRI signal using Monte-Carlo approach or finite difference methods. A modified Weibel model (23,24) has been used in Refs.(84,144–147). Other examples include porous media approach proposed by Mair et al. (148,149); cylindrical model with semi-spherical alveolar shape and two-dimensional grape-like structures used by Fichele et al. (150); Kitaoka model (three-dimensional labyrinth filling a cubic volume (151)) used by Grebenkov (152); tree-like branching structures used by Verbanck et al. (153,154), Perez-Sanchez et al. (155), Conradi et al. (67), and Bartel et al. (119). Models based on morphological images or high-resolution X-ray tomography were used by Miller et al. (156) and Tsuda et al. (157). A geometrical model utilizing Voronoi meshing techniques (158) was simulated by Plotkowiak et al. (80). These publications provided important insights into gas diffusion properties in lung airways, some of them were discussed in detail by Plotkowiak et al. (80).

For these approaches to become a useful research and clinical tool in studying lungs in health and disease they need to allow solution of the inverse problem—evaluating lung geometrical parameters from specially designed MRI experiments. Such approaches should satisfy at least two requirements. They must reflect salient features of lung microstructure geometry, which affects the MR signal formation and the number of parameters characterizing the lung model should be small enough to be able to be determined from MR data. Currently there is only one approach that meets both criteria—in vivo lung morphometry—that was developed in Refs. (84,144–147). It is based on a well-accepted Weibel geometrical model of lung microstructure at the acinar level that is based upon stereological methods (23,24) and theoretical equations relating MR diffusion signal to acinar airways geometric parameters. Based on multi-b measurements of MR diffusion attenuation of signal (usually five to six b-values (84)), this approach not only provides

information on gas diffusion properties, but more importantly, it allows evaluation of lung geometrical parameters from a rather simple and fast MRI experiment. Theoretical parameters used in this approach also allow calculation of standard lung morphological parameters analogous to those extracted from direct histological measurements, hence the term “in vivo lung morphometry.” Details on multi-b sequence requirements and optimization are provided in Refs. (145,147).

IN VIVO LUNG MORPHOMETRY TECHNIQUE

Lung Geometrical Model (Weibel Model) as a Basis for In Vivo Lung Morphometry

To better understand the relationship between the measured ADC and lung microstructure at the alveolar level, we first need to describe lung in terms of some basic geometrical elements. The structure of lung airways is usually considered as a branching tree structure (22) or as confluent rivers (159) beginning at the trachea and leading through bronchi and bronchioles to the terminal bronchiole that feeds each acinus—the major gas exchange unit in the lung. In humans there are 14 generations of airways before the terminal bronchioles and another nine inside the acinus, with an average acinar volume of about 187 mm^3 (22). Gas ventilation in the trachea, bronchi, bronchioles, and terminal bronchioles occurs by convection (bulk flow), while diffusion is the primary ventilation mechanism beyond the terminal bronchioles—in the acini, where about 90 to 95% of gas resides (160). Functionally, the acinus is defined as the largest airway unit in which all airways participate in gas exchange (22). Geometrically, it represents the complex of all airways distal to a terminal bronchiole, starting with a first order respiratory bronchiole. A large number of studies have been devoted to acinar geometry (see for example (23,161–163)). According to (23,24) essentially all airways in the acinus are decorated by alveoli forming an alveolar sleeve (see example in Fig. 6).

In humans, the intra-acinar airways branch dichotomously over about nine generations. Both the internal acinar airway radius r and the outer radius R (including the sleeve of alveoli) vary depending on the position and branching level of the acinar airway tree; however, the variation is rather small—the standard deviation for R is about 60 μm and for r is about 30 μm with mean values of 350 μm and 160 μm correspondingly (23). The “narrowness” of the distributions of parameters R and r creates a solid basis for characterizing acinar airways by the mean values of R and r.

Another important parameter in Figure 6 is the “effective alveolar diameter” L, which is not specified in Ref. 23. To establish a relationship between L and airway radius R we need to further specify the distribution of alveoli in the acinar airways. Numerous models have been proposed previously (see for example Fig. 41 in Ref. 21 and discussion therein). Here we adopt a model in which each alveolus occupies 1/8 of the annular ring (eight-alveolar model (164,165)). In this model we also assume that the alveolar effective diameter L is equal to the length of the cord corresponding to 1/8 of the annular ring, $L = 2R \cdot \sin(\pi/8) = 0.765R$ reducing the number of geometrical parameters in the model to only two: R, and the depth of alveolar sleeve $h = R - r$. If we scale the values from (23) collected at 0.9 TLC (total lung capacity) to 0.6 TLC (usually quoted in the literature) and make the realistic assumption that lung volume scales as the cube of linear dimensions, the mean values of the parameters

become $R = 300$ μm, $r = 140$ μm, and $L = 230$ μm. These results are consistent with literature values for average alveolar diameter ranging from 200 to 260 μm (21,25–27). Models that instead contain four or six alveoli per annular ring would correspond to bigger alveolar diameters (472 and 314 μm, respectively) and do not match the above mentioned experimental data.

Using these parameters, we can estimate the alveolar surface area S_a, lung volume per alveolus V_a, alveolar number density N_v—the number of alveoli per unit lung volume based upon geometry, and the mean linear intercept L_m (146) (see Supporting Information):

$$S_a = \frac{\pi}{4} R \cdot L + \frac{\pi}{4} h \cdot (2R - h) + 2h \cdot L, \qquad V_a = \frac{\pi}{8} R^2 L$$
$$L = 2R \cdot \sin\frac{\pi}{8}, \qquad N_v = \frac{1}{V_a}, \qquad S / V = S_a / V_a = 4 / Lm \qquad [3]$$

Theory of Gas Anisotropic Diffusion in Acinar Airways as a Background for Lung Morphometry Technique

It is important to emphasize that the diffusion time Δ used for lung morphometry technique is a crucial parameter and only the specified diffusion time interval should be used in experiments (145–147). This parameter is selected such that the corresponding r.m.s. free displacement in one direction, $(2D_0 \cdot 2\Delta)^{1/2}$, should be larger than the average alveolar radius but smaller than the mean length of alveolar ducts or alveolar sacs (in human lung, about 0.76 mm and 1 mm, correspondingly (23)). In other words, diffusing gas atoms are expected to diffuse away from single alveoli but remain mostly in the same alveolar duct or sac throughout the duration of the bipolar diffusion-sensitizing gradient pulse – i.e., 2Δ should be short enough but not too short. Since the diffusion coefficient D_0 is different for ^{3}He and ^{129}Xe, and also depends on gas concentration in lung airspaces (see Supporting Information), this diffusion time should be selected for each specific experimental condition. For ^{3}He in human lungs this sets the upper limit of diffusion time Δ to ~1.8 ms for highly diluted ^{3}He gas ($D_0 = 0.88 cm^2/s$) and to ~0.8 ms for lungs filled with pure ^{3}He gas ($D_0 = 2$ cm^2/s). For ^{129}Xe gas, this limit is ~10 ms for highly diluted ^{129}Xe gas ($D_0 = 0.14$ cm^2/s) and 24 ms for pure ^{129}Xe ($D_0 = 0.06$ cm^2/s). In small animal lungs, where the alveolar ducts and sacs are shorter, the diffusion time Δ should be much shorter (147,166–168). This constraint recognizes acinar airways (respiratory broncheoli, alveolar ducts and alveolar sacs) as the elementary geometrical units contributing to the gas diffusion MR signal. Under these conditions, the branching structure of acinar airways play little role in diffusion MR signal formation (145) (see also the detailed discussion later in this review).

The alveolar walls as well as the walls of alveolar ducts and other branches of the airway tree serve as obstacles to the path of diffusing atoms and reduce the gas diffusivity. Crucially, these restrictions are substantially less along the airway axis than perpendicular to it; consequently, diffusion in the airway is anisotropic (84). Therefore, the ADC describing signal attenuation in a single airway depends on the angle α between the direction of the diffusion-sensitizing gradient G and the airway's principal axis:

$$S = S_0 \cdot \exp(-b \cdot \mathrm{ADC}(\alpha)) \quad [4]$$

Due to the cylindrical symmetry of the airway,

$$\mathrm{ADC}(\alpha) = D_{\mathrm{L}} \cos^2 \alpha + D_{\mathrm{T}} \sin^2 \alpha \quad [5]$$

where apparent diffusion coefficients, longitudinal D_{L} and transverse D_{T}, correspond to diffusion along the airway principal axis and in the transverse plane, respectively (84).

With the spatial resolution of several millimeters currently available with ^{3}He or ^{129}Xe MRI, each voxel contains hundreds of airways with different orientations. Due to the large number of acinar airways in each imaging voxel, their orientation distribution function can be taken as uniform, and the total signal S can be written as (84):

$$\begin{aligned} S(b) &= S_0 \exp(-bD_{\mathrm{T}}) \left(\frac{\pi}{4bD_{\mathrm{AN}}} \right)^{1/2} \cdot \Phi\left[(bD_{\mathrm{AN}})^{1/2} \right], \\ D_{\mathrm{AN}} &= D_{\mathrm{L}} - D_{\mathrm{T}} \end{aligned} \quad [6]$$

where $\Phi(x)$ is the error function. This macroscopically isotropic but microscopically anisotropic model predicts non-exponential dependence of diffusion attenuated MRI signal on b-value. The validity of Eq. [6] was confirmed in vivo by experimental measurements in humans (84,146), canines (101), mice (166,167), and rats (127,168) using hyperpolarized ^{3}He gas. It was also recently confirmed in humans (169,170) and rats (132,140) using hyperpolarized ^{129}Xe gas. Example of the data obtained by Jacob et al. from a rat for a broad range of b-values up to 40 s/cm^2 (127) is shown in Figure 7 where the authors compared fitting their data to the model in Eq. [6], a kurtosis model $S(b) = S(0) \cdot \exp[-bD + K/6 \cdot (bD)^2]$, and a monoexponential ADC model, Eq. [2].

Importantly, the diffusivities D_{L} and D_{T} determined from the MR experiment depend on both lung microstructure and the details of the Stejskal-Tanner pulse sequence (144) (therefore they are termed “apparent” diffusivities, ADC). Although general expressions for D_{L} and D_{T} are unavailable, it was demonstrated by means of computer simulations (144–147) that in a physiological range of geometrical parameters r and R, and “realistic” gradients used in MRI experiments, a linear approximation with respect to b-values is sufficient to describe the dependence of apparent diffusion coefficients D_{L} and D_{T} on b-values:

$$\begin{aligned} D_{\mathrm{L}} &= D_{\mathrm{L0}} \cdot (1 - \beta_{\mathrm{L}} \cdot bD_{\mathrm{L0}}) \\ D_{\mathrm{T}} &= D_{\mathrm{T0}} \cdot (1 + \beta_{\mathrm{T}} \cdot bD_{\mathrm{T0}}) \end{aligned} \quad [7]$$

The dimensionless coefficients β_L and β_T reflect the non-Gaussian diffusion effects in each individual airway and are usually defined in terms of the so-called kurtosis K—the second-order term in the general cumulant expansion of the MR signal (e.g., (171–174)); ($K_L = 6\beta_L$, $K_T = -6\beta_T$). It should be noted that the signal $S(b)$ in Eq. [6] also demonstrates "primary" non-monoexponentiality in b-value, which is due to orientation averaging of the signals from individual airways. The non-monoexponentiality in b-value described by the coefficients β_L and β_T is a feature of individual airways and is additional to this "averaging" effect.

Lung Morphometry with Hyperpolarized ^{3}He Gas

In Ref. 146, using the method developed in Ref. 144, the apparent diffusion coefficients D_L and D_T characteristic of ^{3}He gas diffusion were related to the geometrical parameters of acinar airways, R and r, in human lungs by means of phenomenological expressions:

$$\begin{aligned} \frac{D_{L0}}{D_0} &= \exp[-2.89 \cdot (h/R)^{1.78}], \\ \beta_L &= 35.6 \cdot (R/L_1)^{3/2} \cdot \exp[-4/\sqrt{h/R}] \end{aligned} \quad [8]$$

$$\begin{aligned} \frac{D_{T_0}}{D_0} &= \exp[-0.73 \cdot (L_2/R)^{1.4}] \cdot [1 + u(h,R)] \\ u(h,R) &= \exp\left(-A \cdot (h/R)^2\right) \cdot \left[\exp\left(-5(h/R)^2\right) + 5 \cdot (h/R)^2 - 1\right] \\ A &= 1.3 + 0.25 \cdot \exp[14 \cdot (R/L_2)^2] \end{aligned} \quad [9]$$

Here $L_1 = (2D_0\Delta)^{1/2}$ and $L_2 = (4D_0\Delta)^{1/2}$ are the characteristic free-diffusion lengths for one- and two-dimensional diffusion, respectively. In the physiological range ($h/R < 0.6$), parameter β_T remains practically constant at approximately 0.06. The relationships in Eqs. [8] and [9] are illustrated in Supporting Information. Diffusion coefficient D_0 in these equations should also be used according to gas mixture in the lungs (see Supporting Information). For a typical human experiment where about 0.5 L of ^{3}He gas is inhaled to a total lung volume of about 4 L D_0 is 0.93 cm^2/s.

Fitting Eqs. [6-9] to multi-b measurements of the ^{3}He diffusion-attenuated MRI signal in lung airways on a voxel-by-voxel basis makes possible the evaluation of mean geometrical parameters for lung acinar airways (in spite of the airways being too small to be resolved by direct imaging). As a result, parametric maps for airway radii R and alveolar depths h and physiologically important parameters L_m, S/V, and N_v can be generated.

It is important to emphasize that the phenomenological expressions, Eqs. [8] and [9], are not universal, they are derived for specific values of model parameters and diffusion time Δ. Namely, they are valid with accuracy of a few percent for Δ = 1.5 to 2 ms and R = 280 to 400 μm (145). This interval of R covers both the typical radii of acinar alveolar ducts in healthy human lungs and those in lungs with mild emphysema. For larger R corresponding

to lungs with advanced emphysema our approach can produce larger estimation errors and the Weibel geometrical representation of lung airways used in our approach also may become inadequate due to lung tissue destruction. For airway sizes characteristic of small animal lungs (mice, rats), where a typical radius is substantially smaller (R = 100 μm) a modified version of Eqs. [8] and [9] were derived (166) for the diffusion time Δ = 0.3 to 0.4 ms. The corresponding expressions are provided in Supporting Information to this article.

Lung Morphometry with Hyperpolarized ^{129}Xe

To develop the lung morphometry technique with hyperpolarized ^{129}Xe, we need to take into account differences in magnetic and diffusion properties of ^{129}Xe as compared with ^{3}He gas. With proper selection of ^{129}Xe diffusion time, Eqs. [6] and [7] can still be used, but Eqs. [8] and [9] should be modified due to the differences in the gyromagnetic ratios (γ = 7.452 rad/(G ms) for ^{129}Xe vs. γ = 20.379 rad/(G ms) for ^{3}He) and in the free diffusion coefficients (D_0 = 0.88 cm^2/s for diluted ^{3}He in air vs. D_0 = 0.14 cm^2/s for diluted ^{129}Xe in air). Generally speaking, one can modify the gradient pulse sequence parameters (diffusion time Δ, gradient amplitude G_m) in such a way that the dimensionless combinations R/L_1 and bD_0 would be the same as for ^{3}He (147). For a typical gas mixture in human lungs (1 L of ^{129}Xe + 3 L of air), the ^{129}Xe diffusion coefficient D_0 is about 0.1 cm^2/s (see Supporting Information). Hence diffusion time Δ should be increased by a factor of 9. However this would lead to a substantial increase in the imaging time and signal loss due to T2* decay of the MR signal. To address these issues, it was proposed in Ref. 147 to use a smaller diffusion time by simultaneously increasing the diffusion gradient strength. For state-of-the-art human scanners allowing diffusion gradient strengths up to 30–40 mT/m, as shown in Ref. 147, the “optimal” value of the diffusion time is Δ = 5ms , while for small animal scanners, allowing 10-fold stronger gradients, this time is about 1 ms. In Ref. 147, phenomenological expressions similar to Eqs. [8] and [9] were derived for ^{129}Xe gas both for humans and small animals. Corresponding equations are provided here in Supporting Information, Eqs. [S5] to [S7]. However, further theoretical and experimental studies are needed to optimize the parameters of multi-b sequences for the lung morphometry technique with hyperpolarized ^{129}Xe gas.

It should also be noted that the gas concentration may vary across the lung which could lead to bias in estimating both standard ADC values and lung morphometric parameters. This effect could be especially pronounced for ^{129}Xe gas due to its higher atomic weight and viscosity.

Validation of ^{3}He Lung Morphometry Technique

In Ref. 146 the MRI-based measurements of lung morphometric parameters were validated in explanted human lungs against direct invasive morphometric measurements, the current gold standard. The results, shown in Figure 8, demonstrate images of L_m in healthy lungs and lungs with different levels of emphysema (mild, moderate, and severe). Figure 8 also demonstrates an excellent agreement between direct histological and ^{3}He-based measurements of L_m. It should be noted that the MRI experiment provides for much higher statistical power since the data are collected from practically the entire lung as compared with very few regions (20 to 40) from histological cores.

The variation of ADC, anisotropic diffusion coefficients (D_{L0} and D_{T0} from Eqs. [8] to [9]) and acinar airway geometrical parameters with histological emphysema severity, obtained from six lung specimens (146), are shown in Figure 9.

Figure 9a demonstrates that the longitudinal diffusivity D_{L0} grows rapidly at initial stages of emphysema and soon approaches the "free" limit (about 0.88 cm^2/s) for severe cases. Such a behavior is the result of reduced alveolar sleeve depth h with emphysema progression, as seen in Figure 9b. This destruction or retraction of the septa separating alveoli belonging to the same airway leads to lessening of the restrictions to ^{3}He gas diffusion along (parallel to) airways, practically removing them in severe emphysema cases.

Figure 9b demonstrates that the major decrease of alveolar depth occurs already at the initial stages of emphysema—between normal and mild stages. At the same time, the airway radius R grows substantially with emphysema progression, reflecting tissue dilation and alveolar destruction and coalescence. The mechanism of "dilation of alveolar ducts with retraction of alveolar walls" was first suggested decades ago to describe the microscopic appearance of emphysema in human lungs (164) and was later confirmed in elastase-induced emphysema in rodents (175,176). More recent studies (177) also demonstrated shortening of alveolar walls and effacement of inter-alveolar septa. The results in Ref. 146 observed this phenomenon by a non-invasive technique for the first time and quantified such changes with emphysema progression.

The results for surface-to-volume ratio from diffusion MRI shown in Figure 9c are in good agreement with the results of morphometric measurements (17) obtained from excised lung specimens: $S/V = 256 \pm 24$ cm^2/mL for control human subjects, 165 ± 23 cm^2/mL for subjects with mild emphysema, and 43 ± 6 cm^2/mL for severe emphysema.

Measurements of N_v in two healthy lung specimens (120 and 146 per mm^3) in Figure 9d are in agreement with a direct morphometric approach (26) in healthy human lungs (the average N_v varies between 132 and 177 per mm^3). In addition to the above-cited measurements in healthy lungs, data in Figure 9d demonstrate changes in the number density of alveoli with emphysema progression—N_v decreases to about 60 per mm^3 in mild emphysema and even further to about 10 per mm^3 in lungs with severe emphysema. Such decreases in alveolar density are expected due to lung dilation and alveolar coalescence.

Osmanagic et al. (166) applied the lung morphometry technique with hyperpolarized ^{3}He diffusion MR to study explanted lungs in mice. The MR protocol and empirical relationships relating diffusion measurements to geometrical parameters of lung acinar airways were adjusted to acquire data with much shorter diffusion times as compared with humans to accommodate the substantially smaller acinar airway length. This measurements yielded mean values of lung surface-to-volume ratio of 670 cm^{-1}, alveolar density of 3200 per mm^3, alveolar depth of 55 μm, and mean chord length of 62 μm, all consistent with various results from the literature obtained by stereological analysis of mouse lungs (40,178–185). The technique was further implemented by Wang et al. (167) for in vivo lung imaging in mice. Results indicated a very good agreement between in vivo morphometry via ^{3}He MRI and microscopic morphometry after sacrifice.

Application of In Vivo Lung Morphometry to Study Human and Animal Lungs

Quirk et al. (104) used the in vivo ^{3}He lung morphometry technique to quantitatively characterize early emphysematous changes in lung microstructure of current and former smokers. Thirty subjects with over 30 pack-year histories and mild or no abnormalities on pulmonary function tests (PFT) were studied. The results were compared against clinical standards: PFT and low-dose computed tomography (CT). Results (see Fig. 10) demonstrate that the non-invasive ^{3}He lung morphometry detected alterations in acinar structure in smokers with clinically normal PFTs. Compared with smokers with FEV_a/FVC >80 %, those with COPD (FEV_a/FVC <70 %) had statistically significantly reduced alveolar depth h (0.07±0.02 vs. 0.13±0.02 mm, $P = 0.016$) and enlarged acinar ducts radius R (0.36±0.02 vs. 0.304±0.005 mm, $P = 0.016$). The mean alveolar geometry measurements in the healthiest subjects were in excellent quantitative agreement with literature values obtained using invasive techniques (R = 0.30 mm, $h = 0.14$ mm at 1 L above FRC (23)). Importantly, ^{3}He lung morphometry detected greater abnormalities than either PFT or CT.

The important feature of all these maps is their relative homogeneity in the GOLD 0 former smoker's lungs versus significant disease-related heterogeneity even in early emphysema. In the latter case a clear contrast is seen between central portion of the lung and lung periphery. This "bimodal" behavior (two-peak feature) is especially obvious if data are presented as histograms, as in Figure 11.

First we note that while lung density reflected in CT histogram is different in emphysema as compared with normal lungs, the relative shift in practically all parameters determined by ^{3}He MRI is substantially larger. Probably the most interesting is behavior of L_m that demonstrates a pronounced "bimodal" feature that is also seen in alveolar depth histogram and only hinted in other ^{3}He-derived parameters, but is not seen in CT data at all.

Another population where one expects a change in alveolar microstructure is post pneumonectomy. After removal of a lung, the remaining lung usually increases in size to fill the space in the thoracic cavity. While the extent of this increase depends on the shifting of other organs, primarily the heart and liver, some degree of expansion is commonly noted. When the lung increases in size, it is uncertain whether this is the result of stretching of the existing alveoli, the growth of new alveoli, or a combination of both effects. If the lung responded purely by stretching, we would expect that the number of alveoli would be the same as for a single lung, the alveolar number density N_v would decrease, and the values of R and L_m would be elevated. A recent study by Butler et al. (186) using helium lung morphometry found that a woman 15 years post pneumonectomy had normal values for R with a uniform distribution of values across the lung, and slightly decreased values for h. These results suggest that the lung responded to the mechanical forces by forming new alveoli. These results were supported by Wang et al. (187) in a longitudinal mouse study where compensatory growth was found to restore the lung volume, compliance, and alveolar number to pre-surgery values by a month following surgery.

Hajari et al. (188) used in vivo lung morphometry to study the mechanisms of lung inflation and deflation in humans. Despite decades of research, there is little consensus about whether lung inflation occurs due to the recruitment of new alveoli or by changes in the size and/or

shape of alveoli and alveolar ducts. In this study Hajari et al. measured the average alveolar depth and alveolar duct radius at three levels of inspiration in five healthy human subjects and calculated the average alveolar volume, surface area, and the total number of alveoli at each level of inflation. The results indicated that during a 143 ± 18 % increase in lung gas volume, the average alveolar depth decreases 21 ± 5 %, the average alveolar duct radius increases 7 ± 3 %, and the total number of alveoli increases by 96 ± 9 % (results are means ± SD between subjects). These results indicated that in healthy human subjects the lung inflates primarily by alveolar recruitment and, to a lesser extent, by anisotropic expansion of alveolar ducts.

The first ^{129}Xe applications of in vivo lung morphometry technique have been demonstrated by Ruppert et al. (169) (see example in Fig. 12) and Ouriadov et al. (170) in humans, and Boudreau et al. (132), and Hegarty et al. (140) in rats.

Accuracy of In Vivo Lung Morphometry Technique: Effects of Acinar Airways Branching and Distribution of Airway Geometrical Parameters (Theoretical Analysis)

While lung morphometry technique with hyperpolarized ^{3}He diffusion MRI has been validated experimentally in human (146) and mice (166,167) lungs, questions related to its “theoretical accuracy” were discussed in detail by Sukstanskii et al. in Ref. 145. As for any approach dealing with a complicated structure, the lung morphometry technique with hyperpolarized gas diffusion MRI is based on assumptions and simplifications that potentially might bias the measurements. The core of the technique is a model that incorporates the salient feature of gas diffusion in acinar airways on the time scale when diffusing gas molecules have a chance to diffuse in and out from single alveoli but still spend most of their time in the same acinar airway. This leads to diffusion being anisotropic on microscopic (single airway) scale-the diffusivity D_{L} along airway axis is bigger than the diffusivity D_{T} perpendicular this axis. Since the measured MR signal originates from a large number of acinar airways with almost homogeneous distribution of their direction, diffusion MR signal has very little dependence on diffusion sensitizing gradient direction, i.e. it has macroscopically isotropic character. This microscopically anisotropic feature of the technique has been confirmed in numerous publications (84,101,127,132,146,166–169).

To address the accuracy of this theoretical model, Sukstanskii et al. (145) conducted Monte-Carlo simulations of gas diffusion in lung acini in a more general model, accounting for (a) the branching structure of the acinar airways and the finite length of alveolar ducts and sacs, (b) the distribution of airway geometrical parameters R and r of 17 % about the mean values, and (c) the effects of internal inhomogeneous magnetic fields. These results were then fitted by the model in Eqs. [6] to [9].

Simulations were conducted for diffusion time Δ = 1.8 ms used in ^{3}He lung morphometry technique in humans (146). For this short diffusion time the probability to cross two branching nodes and to diffuse into the next-to-adjacent airway is negligibly small—about 1 %. Hence it is sufficient to consider for simulations only two types of basic airway configurations as shown in Figure 13 and weight them appropriately for calculating MRI signal. Of course, such a simplification is not valid for long diffusion times.

The input values of the geometrical parameters (typical for healthy lungs and lungs with mild emphysema) used in simulations and those from the fits to the data are presented in Table 1. For SNR equal or bigger than 100, fitting differences associated with noise are much smaller than that related to other sources.

According to Table 1, all the parameters (R, r, S/V) found from fitting the model to simulated data using Eqs. [6] to [9], representing an idealized structure of branching acinar airways, are very close to the input values. In particular, for the surface-to-volume ratio, the average difference is 6.5 %. For a non-invasive technique able to measure microstructural parameters across the lung, this degree of potential error is easily tolerable.

One of the main assumptions of the model was the ability to describe the total MR signal from an acinus as the sum of signals from individual acinar airways. This assumption holds only if a diffusing ^{3}He atom resides primarily within the same airway throughout the diffusion gradient pulse. Our simulations demonstrate that ^{3}He atoms spend most of their diffusion time (typically, 75%) within a single airway. This may explain why our approach, based on the assumption of “noncommunicating” or infinite-length airways, describes data very well, as shown in Table 1. It is important to emphasize once again that only specified diffusion times should be used when applying lung morphometry technique. For example, applying this technique to study human lungs using hyperpolarized ^{3}He gas with diffusion times different than those prescribed in Ref. 146 (1.6–1.8 ms) may lead to bias in estimates of lung geometrical parameters.

ADC VERSUS LUNG MORPHOMETRY WITH HYPERPOLARIZED GAS–AMBIGUITY OF ADC RELATIONSHIP WITH LUNG MICROSTRUCTURE

As mentioned in the Introduction, ADC is an important but insufficient parameter to characterize lung microstructure in standard morphometric terms because there is no one-to-one correspondence between ADC and histological parameters, e.g., L_m. To demonstrate this, in Figure 14 (adapted from Ref. 189, the results of the study (104) for 30 subjects are accumulated and plotted as ADC vs. Lm (all data for diffusion time 1.8 ms). The lines represent the dependence of ADC as a function of mean linear intercept L_m, theoretically calculated at fixed values of the ratio h/R (given by numbers near the lines) by using Eqs. [8], [9] and

$$\mathrm{ADC} = \frac{1}{3}D_{L0} + \frac{2}{3}D_{T0} \quad [10]$$

As we see, each value of L_m can be associated with numerous values of ADC, and vice versa. It means that the correlation between these two parameters is very limited.

LONG-RANGE DIFFUSION

All of the methods discussed above have used diffusion times of about 2 ms, corresponding to free displacements under 1 mm. Thus, most gas atoms start and end the diffusion-interval

(determined by the gradient pulse) in the same acinar airway. Additional information about the lung airways is available from long-range ADC (LRADC) measurements.

Diffusion over longer distances (1–3 cm, for example) requires much longer diffusion time intervals (several seconds). This is much longer than the intravoxel $T2^*$ of approximately 20 ms at 1.5 T, which determines the life-time of transverse magnetization in gradient-echo images. The solution is to let the longitudinal spin magnetization M_z carry the position information. To achieve this, a sequence of two $\pi/4$ RF pulses is used, separated by a gradient pulse in the x-direction (116). The M_z is modulated from relative value 1 to 0 as a function of x,

$$M_z = \frac{1}{2}[1 - \cos(2\pi x/\lambda)] \quad [11]$$

where the wavelength of modulation λ is determined by the area of the gradient pulse $\lambda = 2\Pi/\gamma Gt$. A small-flip angle inspection image taken afterwards in the XY plane reveals a stripe pattern superimposed on the lung image. An example of stripe images obtained from a dog with unilateral elastase-induced emphysema is shown in Figure 15.

Brownian motion (diffusion) of the gas will mix the bright (magnetized) and dark (unmagnetized) spins, leading to a decay of the spatial modulation (115). That is, the stripes fade without losing average intensity, as in Figure 15. To reveal only the effect of diffusion on the stripes, a normalizing scheme that corrects for overall T_1 decay of the signal as well as consumption of M_z by the RF imaging pulses is usually used (67,116,117).

Woods et al. (116) found that in healthy canine lungs the average LRADC was $0.015\pm0.004 cm^2/s$, which is about 10 times smaller than the average measured value for the traditional short-range ADC measured over milliseconds and hundreds of microns. In the emphysematous lung, the average LRADC varied from animal to animal, with significant increases from the normal lung in four of five dogs. An average increase in LRADC by a factor of 2.7 in the emphysematous canine lungs implies that the technique may be used as a measure of tissue destruction, airway connectivity, and collateral ventilation over large distances.

The relevant length scale for diffusive motion is $\lambda/2$, about 1 to 1.5 cm in Ref. 116. In healthy lungs, the airways form a network of bifurcating paths over about 23 levels (21). Thus the airways are singly connected with a unique path between any two points: a journey from one location at, e.g., level 21 to level 22 at a point 1.5 cm away necessarily requires going from one acinus to another, since acini have maximum linear dimensions of about 7 mm. Thus, the atom must move from level 21 to at least level 16 (the level where acini commence and interconnect) and back to level 22. At each of many junctions, the atom must make the correct turn if it is to leave its starting acinus. This tortuous path will make the long-range ADC quite small ($0.02 cm^2/s$ has been measured in vivo in normal human lungs) if gas motion is restricted to along the airway tree. Further discussion of the diffusion physics behind LRADC measurements can be found in Refs. 67,119,153,154,190.

In emphysema, collateral ventilation pathways develop and can become as important for peripheral gas flow as the more usual (airway) routes (191–193). This occurs as some collateral paths will have less resistance to gas flow than through diseased airways, allowing for ventilation and gas exchange to partially adapt to the structural and physiological abnormalities imposed by the disease. Thus, there are now an increased number of diffusion paths that are functioning routes for long-distance convective transport or diffusion of gas. In essence, collateral paths are short-circuits (bypasses) and will result in substantial increase in the long-range diffusivity. Thus, we believe that long-range ADC measurements provide information on the extent of collateral pathways.

Increased collateral ventilation will be required for the success of some (although not all) airway bypass procedures proposed to ameliorate emphysema. In one such scenario (194), an artificial airway is made by piercing an airway wall to connect a patent airway to a previously under-ventilated or gas-trapped region of lung parenchyma. The desired situation is that a large volume of hyperinflated lung that intercommunicates effectively through collateral pathways could be emptied through a small number of artificial airways, producing many of the benefits of lung volume reduction surgery but with minimal invasiveness. Without collateral paths, this proposed procedure is unlikely to succeed, as only the region immediately adjacent to the connection to the new airway would be emptied of its trapped gas.

Different approaches to studying LRADC have also been published. Fichele et al. proposed monitoring filling-in of magnetization from neighboring slices (195). Mugler et al. (196) and Wang et al. (120) have used through-slice magnetization modulation reporting measurements for diffusion times ranging from milliseconds to seconds. In healthy subjects, they found that the apparent diffusion coefficient decreased by about 10-fold, from approximately 0.2 to 0.02 cm^2/s, as the diffusion time increased from approximately 1 ms to 1 s. Such a decrease is similar to result by Woods et al. (116). Boudreau et al. (132) used PGSE method at low static magnetic field strength of 73.5 mT for diffusion measurements at Δ = 6, 50, and 100 ms.

CONCLUDING REMARKS

Numerous diagnostic tools have been developed to evaluate the presence and the stage of chronic obstructive pulmonary diseases. The introduction of hyperpolarized gas MRI (^{3}He and ^{129}Xe) has opened the door to developing new diagnostic tools for studying lung function and structure. Most applications to date have used hyperpolarized ^{3}He as it has a higher nuclear magnetic moment than^{129}Xe (thus providing stronger MRI signal), is easier to polarize and is more biologically inert. However, a major problem tempering clinical implementation of hyperpolarized ^{3}He gas MRI techniques is a shortage of the gas and its increasing cost (197), although recapture/reuse systems are being implemented (198) and will help to extend the gas supply. An alternative “hyperpolarizable” gas, ^{129}Xe, is cheaper and more readily available suggesting that it can become the gas of choice for these new techniques.

In this review we discussed MRI methods that are based on measurements of hyperpolarized gas (^{3}He or ^{129}Xe) diffusion in the lung airspaces of humans and animals. These methods, being sensitive to changes in lung microstructure at the alveolar level, have a great potential to improve our understanding of lung structure and function in health and disease.

Numerous studies have demonstrated changes in hyperpolarized gas ADC in different diseases, especially in emphysema suggesting the use of ADC as a biomarker for disease progression. Advantages of the ADC approach are its relative simplicity and speed (only two *b*-values are needed for measurement as compared with minimum three for lung morphometry). However, the ADC is not an inherent property of the lung microstructure (as is L_m) and depends on the details of MRI protocol (diffusion time and *b*-value) that are not always described in scientific publications. This makes it impossible to directly compare data from different laboratories. Establishing guidelines for studying lung with hyperpolarized gases, similar to those established by the American Thoracic Society and European Respiratory Society for lung morphometry (31), would be of great value. Part of this effort should also be standardizing breathing protocols as MRI measurements substantially depend on lung volume.

An advanced technique-in vivo lung morphometry-allows evaluation of the geometrical parameters of acinar airways and alveoli from hyperpolarized gas diffusion MRI measurements. It reports on lung microstructure using data metrics (L_m, S/V, alveolar density, acinar airways radii) that are established markers used by lung physiologists for decades but were previously available only from invasive biopsy studies. Compared with PFTs that provide only “global” assessment of the disease, in vivo lung morphometry offers three-dimensional tomographic information on lung microstructure and may substantially aid in accurate diagnostic and treatment options. Compared with CT (which provides information only on lung tissue density and may be used to infer aspects of lung structure), in vivo lung morphometry provides information on gas ventilation and tissue microstructure at the alveolar level without the use of ionizing radiation. The safety and sensitivity of this technique suggests that it is well suited to improving our understanding of the mechanisms and development of pulmonary diseases and has the potential for monitoring the efficacy of therapeutic interventions in clinical trials.

Another issue that can streamline the adoption of hyperpolarized gas MRI into the clinical arena is accelerating data acquisition. For example, such techniques as radial acquisition (e.g. (199)) or widely available parallel imaging can substantially speed up clinical protocols potentially allowing whole lung coverage within a few seconds easily tolerable for breath-hold sessions. Both ADC and lung morphometry techniques could benefit from these advances.

Supplementary Material

Refer to Web version on PubMed Central for supplementary material.

ACKNOWLEDGMENTS

The authors acknowledge helpful discussions and long and productive collaboration with Drs. David Gierada, Joel Cooper, Steve Lefrak, Ewald Weibel, James Hogg, Robert Senior, Mike Holtzman, Barbara Lutey, Rich Pierce, Yulin Chang, Bryan Meyers, and Alexander Patterson.

Grant sponsor: NIH; Grant numbers: R01HL70037; R01 HL 72369, and P50 HL084922

REFERENCES

1. Rabe KF, Hurd S, Anzueto A, et al. Global strategy for the diagnosis, management, and prevention of chronic obstructive pulmonary disease: GOLD executive summary. Am J Respir Crit Care Med 2007;176:532–555. [PubMed: 17507545]
2. Mead J, Turner JM, Macklem PT, Little JB. Significance of the relationship between lung recoil and maximum expiratory flow. J Appl Physiol 1967;22:95–108. [PubMed: 6017658]
3. Hogg JC, Macklem PT, Thurlbeck WM. Site and nature of airway obstruction in chronic obstructive lung disease. New Engl J Med 1968;278:1355–1360. [PubMed: 5650164]
4. Van Brabandt H, Cauberghs M, Verbeken E, Moerman P, Lauweryns JM, Van de Woestijne KP. Partitioning of pulmonary impedance in excised human and canine lungs. J Appl Physiol 1983;55:1733–1742. [PubMed: 6662764]
5. Yanai M, Sekizawa K, Ohrui T, Sasaki H, Takishima T. Site of airway obstruction in pulmonary disease: direct measurement of intrabronchial pressure. J Appl Physiol 1992;72:1016–1023. [PubMed: 1568955]
6. Snider GL. Emphysema: the first two centuries–and beyond. A historical overview, with suggestions for future research: Part 2. Am Rev Respir Dis 1992;146:1615–1622. [PubMed: 1456587]
7. Gelb AF, Hogg JC, Muller NL, et al. Contribution of emphysema and small airways in COPD. Chest 1996;109:353–359. [PubMed: 8620705]
8. Churg A, Tai H, Coulthard T, Wang R, Wright JL. Cigarette smoke drives small airway remodeling by induction of growth factors in the airway wall. Am J Respir Crit Care Med 2006;174:1327–1334. [PubMed: 17008639]
9. Hogg JC. Pathophysiology of airflow limitation in chronic obstructive pulmonary disease. Lancet 2004;364:709–721. [PubMed: 15325838]
10. Hogg JC, Chu F, Utokaparch S, et al. The nature of small-airway obstruction in chronic obstructive pulmonary disease. New Engl J Med 2004;350:2645–2653. [PubMed: 15215480]
11. Thurlbeck WM. Overview of the pathology of pulmonary emphysema in the human. Clin Chest Med 1983;4:337–350. [PubMed: 6357598]
12. Thurlbeck WM, Simon G. Radiographic appearance of the chest in emphysema. AJR Am J Roentgenol 1978;130:429–440. [PubMed: 415543]
13. Gevenois PA, Yernault JC. Can computed tomography quantify pulmonary emphysema? Eur Respir J 1995;8:843–848. [PubMed: 7656960]
14. Gould GA, MacNee W, McLean A, Warren PM, Redpath A, Best JJ, Lamb D, Flenley DC. CT measurements of lung density in life can quantitate distal airspace enlargement–an essential defining feature of human emphysema. Am Rev Respir Dis 1988;137:380–392. [PubMed: 3341629]
15. Muller NL, Staples CA, Miller RR, Abboud RT. “Density mask”. An objective method to quantitate emphysema using computed tomography. Chest 1988;94:782–787. [PubMed: 3168574]
16. Hayhurst MD, MacNee W, Flenley DC, Wright D, McLean A, Lamb D, Wightman AJ, Best J. Diagnosis of pulmonary emphysema by computerized tomography. Lancet 1984;2:320–322. [PubMed: 6146866]
17. Coxson HO, Rogers RM, Whittall KP, D’Yachkova Y, Pare PD, Sciurba FC, Hogg JC. A quantification of the lung surface area in emphysema using computed tomography. Am J Respir Crit Care Med 1999;159:851–856. [PubMed: 10051262]
18. Lederer DJ, Enright PL, Kawut SM, Hoffman EA, Hunninghake G, van Beek EJ, Austin JH, Jiang R, Lovasi GS, Barr RG. Cigarette smoking is associated with subclinical parenchymal lung

disease: the Multi-Ethnic Study of Atherosclerosis (MESA)-lung study. Am J Respir Crit Care Med 2009;180:407–414. [PubMed: 19542480]

19. Remy-Jardin M, Edme JL, Boulenguez C, Remy J, Mastora I, Sobaszek A. Longitudinal follow-up study of smoker's lung with thin-section CT in correlation with pulmonary function tests. Radiology 2002;222:261–270. [PubMed: 11756735]
20. Soejima K, Yamaguchi K, Kohda E, et al. Longitudinal follow-up study of smoking-induced lung density changes by high-resolution computed tomography. Am J Respir Crit Care Med 2000;161 (Pt 1):1264–1273. [PubMed: 10764322]
21. Weibel ER. Morphometry of the human lung. Springer-Verlag; Berlin, 1963.
22. Weibel E Design of airways and blood vessels considered as branching trees In: Crystal RG, West JB, Barnes PJ, Cherniack NS, editors. The lung: scientific foundations. New York: Raven Press, Ltd.; 1991 pp 711–720.
23. Haefeli-Bleuer B, Weibel ER. Morphometry of the human pulmonary acinus. Anat Rec 1988;220:401–414. [PubMed: 3382030]
24. Mercer RR, Laco JM, Crapo JD. Three-dimensional reconstruction of alveoli in the rat lung for pressure-volume relationships. J Appl Physiol 1987;62:1480–1487. [PubMed: 3597219]
25. Schreider JP, Raabe OG. Structure of the human respiratory acinus. Am J Anat 1981;162:221–232. [PubMed: 7315750]
26. Ochs M, Nyengaard JR, Jung A, Knudsen L, Voigt M, Wahlers T, Richter J, Gundersen HJ. The number of alveoli in the human lung. Am J Respir Crit Care Med 2004;169:120–124. [PubMed: 14512270]
27. Mercer RR, Russell ML, Crapo JD. Alveolar septal structure in different species. J Appl Physiol 1994;77:1060–1066. [PubMed: 7836104]
28. Robbesom AA, Versteeg EM, Veerkamp JH, van Krieken JH, Bulten HJ, Smits HT, Willems LN, van Herwaarden CL, Dekhuijzen PN, van Kuppevelt TH. Morphological quantification of emphysema in small human lung specimens: comparison of methods and relation with clinical data. Mod Pathol 2003;16:1–7. [PubMed: 12527706]
29. Lum H, Huang I, Mitzner W. Morphological evidence for alveolar recruitment during inflation at high transpulmonary pressure. J Appl Physiol 1990;68:2280–2286. [PubMed: 2384408]
30. Weibel ER. What makes a good lung? Swiss Med Wkly 2009;139:375–386. [PubMed: 19629765]
31. Hsia CC, Hyde DM, Ochs M, Weibel ER. An official research policy statement of the American Thoracic Society/European Respiratory Society: standards for quantitative assessment of lung structure. Am J Respir Crit Care Med 2010;181:394–418. [PubMed: 20130146]
32. Ochs M A brief update on lung stereology. J Microsc 2006;222(Pt 3):188–200. [PubMed: 16872418]
33. Weibel ER, Hsia CC, Ochs M. How much is there really? Why stereology is essential in lung morphometry. J Appl Physiol 2007;102:459–467. [PubMed: 16973815]
34. Mitzner W Use of mean airspace chord length to assess emphysema. J Appl Physiol 2008;105:1980–1981. [PubMed: 18719230]
35. Greaves IA. Commentaries on viewpoint: use of mean airspace chord length to assess emphysema. Mean airspace chord length is useful in assessing emphysema. J Appl Physiol 2008;105:1982;
36. Hsia CC, Hyde DM, Ochs M, Weibel ER. Commentaries on viewpoint: use of mean airspace chord length to assess emphysema. To be or not to be-accurate. J Appl Physiol 2008;105:1982–1983;
37. Bates JH. Commentaries on viewpoint: use of mean airspace chord length to assess emphysema. Purists versus pragmatists. J Appl Physiol 2008;105:1983;
38. Rossiter HB, Breen EC. Commentaries on viewpoint: use of mean airspace chord length to assess emphysema. Assessment of emphysema benefits from quantification of heterogeneity. J Appl Physiol 2008;105:1983–1984;
39. Parameswaran H, Majumdar A, Hamakawa H, Suki B. Commentaries on viewpoint: use of mean airspace chord length to assess emphysema. Pattern of parenchymal destruction determines lung function decline. J Appl Physiol 2008;105:1984;
40. Fehrenbach H Commentaries on viewpoint: use of mean airspace chord length to assess emphysema. What does Lm tell us about lung pathology? J Appl Physiol 2008;105:1984–1985;

41. Mata JF. Commentaries on viewpoint: use of mean airspace chord length to assess emphysema. Mean airspace chord length and hyperpolarized gas magnetic-resonance measurements. J Appl Physiol 2008;105:1985; [PubMed: 19140251]
42. Walker TG, Happer W. Spin-exchange optical pumping of noble-gas nuclei. RevModPhys 1997;69:629–642.
43. Leawoods JC, Yablonskiy DA, Saam B, Gierada DS, Conradi MS. Hyperpolarized 3He gas production and MR imaging of the lung. Concepts Magn Reson 2001;13:277–293.
44. Ruset IC, Ketel S, Hersman FW. Optical pumping system design for large production of hyperpolarized xenon. Phys Rev Lett 2006;96:053002. [PubMed: 16486926]
45. Hersman FW, Ruset IC, Ketel S, et al. Large production system for hyperpolarized 129Xe for human lung imaging studies. Acad Radiol 2008;15:683–692. [PubMed: 18486005]
46. Cleveland ZI, Moller HE, Hedlund LW, Driehuys B. Continuously infusing hyperpolarized 129Xe into flowing aqueous solutions using hydrophobic gas exchange membranes. J Phys Chem B 2009;113:12489–12499. [PubMed: 19702286]
47. Lutey BA, Lefrak SS, Woods JC, et al. Hyperpolarized 3He MR imaging: physiologic monitoring observations and safety considerations in 100 consecutive subjects. Radiology 2008;248:655–661. [PubMed: 18641256]
48. Driehuys B, Martinez-Jimenez S, Cleveland ZI, et al. Chronic obstructive pulmonary disease: safety and tolerability of hyperpolarized 129Xe MR imaging in healthy volunteers and patients. Radiology 2012;262:279–289. [PubMed: 22056683]
49. Chen XJ, Chawla LW, Hedlund LW, Moller HE, MacFall JR, Johnson GA. MR microscopy of lung airways with hyperpolarized ^{3}HE. Mag Reson Med 1998;39:79–84.
50. Johnson GA, Cofer GP, Hedlund LW, Maronpot RR, Suddarth SA. Registered (1)H and (3)He magnetic resonance microscopy of the lung. Magn Reson Med 2001;45:365–370. [PubMed: 11241691]
51. Driehuys B, Walker J, Pollaro J, Cofer GP, Mistry N, Schwartz D, Johnson GA. 3He MRI in mouse models of asthma. Magn Reson Med 2007;58:893–900. [PubMed: 17969115]
52. de Lange EE, Mugler JP, Brookeman JR, Daniel TM, Truwit JD, Teates CD, Knight-Scott J. MR Imaging of the lungs with hyperpolarized He3 gas. 1998; 4 p. 18–24.
53. Kauczor HU, Ebert M, Kreitner KF, Nilgens H, Surkau R, Heil W, Hofmann D, Otten EW, Thelen M. Imaging of the lungs using 3He MRI: preliminary clinical experience in 18 patients with and without lung disease. J Magn Reson Imaging 1997;7:538–543. [PubMed: 9170039]
54. Saam B, Yablonskiy DA, Gierada DS, Conradi MS. Rapid imaging of hyperpolarized gas using EPI. Magn Reson Med 1999;42:507–514. [PubMed: 10467295]
55. Salerno M, Altes TA, Brookeman JR, de Lange EE, Mugler JP, III. Dynamic spiral MRI of pulmonary gas flow using hyperpolarized (3)He: preliminary studies in healthy and diseased lungs. Magn Reson Med 2001;46:667–677. [PubMed: 11590642]
56. Deninger AJ, Mansson S, Petersson JS, et al. Quantitative measurement of regional lung ventilation using 3He MRI. Magn Reson Med 2002;48:223–232. [PubMed: 12210930]
57. Deninger AJ, Eberle B, Ebert M, et al. Quantification of regional intrapulmonary oxygen partial pressure evolution during apnea by (3)He MRI. J Magn Reson 1999;141:207–216. [PubMed: 10579944]
58. Fischer MC, Kadlecek S, Yu J, Ishii M, Emami K, Vahdat V, Lipson DA, Rizi RR. Measurements of regional alveolar oxygen pressure using hyperpolarized 3He MRI. Acad Radiol 2005;12:1430–1439. [PubMed: 16253855]
59. Rizi RR, Baumgardner JE, Ishii M, Spector ZZ, Edvinsson JM, Jalali A, Yu J, Itkin M, Lipson DA, Gefter W. Determination of regional VA/Q by hyperpolarized 3He MRI. Magn Reson Med 2004;52:65–72. [PubMed: 15236368]
60. Dregely I, Mugler JP, III, Ruset IC, et al. Hyperpolarized Xenon-129 gas-exchange imaging of lung microstructure: first case studies in subjects with obstructive lung disease. J Magn Reson Imaging 2011;33:1052–1062. [PubMed: 21509861]
61. Dregely I, Ruset IC, Mata JF, et al. Multiple-exchange-time xenon polarization transfer contrast (MXTC) MRI: initial results in animals and healthy volunteers. Magn Reson Med 2012;67:943–953. [PubMed: 22213334]

62. Ruppert K, Brookeman JR, Hagspiel KD, Driehuys B, Mugler JP, III. NMR of hyperpolarized (129)Xe in the canine chest: spectral dynamics during a breath-hold. NMR Biomed 2000;13:220–228. [PubMed: 10867700]
63. Patz S, Muradyan I, Hrovat MI, Dabaghyan M, Washko GR, Hatabu H, Butler JP. Diffusion of hyperpolarized 129Xe in the lung: a simplified model of 129Xe septal uptake and experimental results. New J Phys 2011;13:015009.
64. Chang YV. MOXE: A model of gas exchange for hyperpolarized (129) Xe magnetic resonance of the lung. Magn Reson Med 2012; DOI 10.1002/mrm.24304.
65. Moller HE, Chen XJ, Saam B, Hagspiel KD, Johnson GA, Altes TA, de Lange EE, Kauczor HU. MRI of the lungs using hyperpolarized noble gases. Magn Reson Med 2002;47:1029–1051. [PubMed: 12111949]
66. Hoffman EA, van Beek E. Hyperpolarized media MR imaging–expanding the boundaries? Acad Radiol 2006;13:929–931. [PubMed: 16843844]
67. Conradi MS, Yablonskiy DA, Woods JC, et al. 3He diffusion MRI of the lung. Acad Radiol 2005;12:1406–1413. [PubMed: 16253852]
68. Ishii M, Fischer MC, Emami K, et al. Hyperpolarized helium-3 MR imaging of pulmonary function. Radiol Clin North Am 2005;43:235–246. [PubMed: 15693659]
69. Patz S, Hersman FW, Muradian I, Hrovat MI, Ruset IC, Ketel S, Jacobson F, Topulos GP, Hatabu H, Butler JP. Hyperpolarized (129)Xe MRI: a viable functional lung imaging modality? Eur J Radiol 2007;64:335–344. [PubMed: 17890035]
70. Fain S, Schiebler ML, McCormack DG, Parraga G. Imaging of lung function using hyperpolarized helium-3 magnetic resonance imaging: review of current and emerging translational methods and applications. J Magn Reson Imaging 2010;32:1398–1408. [PubMed: 21105144]
71. Matsuoka S, Patz S, Albert MS, Sun Y, Rizi RR, Gefter WB, Hatabu H. Hyperpolarized gas MR Imaging of the lung: current status as a research tool. J Thorac Imaging 2009;24:181–188. [PubMed: 19704321]
72. Emami K, Stephen M, Kadlecek S, Cadman RV, Ishii M, Rizi RR. Quantitative assessment of lung using hyperpolarized magnetic resonance imaging. Proc Am Thorac Soc 2009;6:431–438. [PubMed: 19687215]
73. Fain SB, Korosec FR, Holmes JH, O'Halloran R, Sorkness RL, Grist TM. Functional lung imaging using hyperpolarized gas MRI. J Magn Reson Imaging 2007;25:910–923. [PubMed: 17410561]
74. van Beek EJ, Wild JM. Hyperpolarized 3-helium magnetic resonance imaging to probe lung function. Proc Am Thorac Soc 2005;2:528–532, 510. [PubMed: 16352759]
75. Altes TA, Salerno M. Hyperpolarized gas MR imaging of the lung. J Thorac Imaging 2004;19:250–258. [PubMed: 15502612]
76. van Beek EJ, Wild JM, Kauczor HU, Schreiber W, Mugler JP, III, de Lange EE Functional MRI of the lung using hyperpolarized 3-helium gas. J Magn Reson Imaging 2004;20:540–554. [PubMed: 15390146]
77. Altes TA, de Lange EE. Applications of hyperpolarized helium-3 gas magnetic resonance imaging in pediatric lung disease. Top Magn Reson Imaging 2003;14:231–236. [PubMed: 12973130]
78. Kauczor HU. Hyperpolarized helium-3 gas magnetic resonance imaging of the lung. Top Magn Reson Imaging 2003;14:223–230. [PubMed: 12973129]
79. Kauczor HU, Eberle B. Elucidation of structure-function relationships in the lung: contributions from hyperpolarized 3helium MRI. Clin Physiol Funct Imaging 2002;22:361–369. [PubMed: 12464138]
80. Plotkowiak M, Burrowes K, Wolber J, Buckley C, Davies R, Gleeson F, Gavaghan D, Grau V. Relationship between structural changes and hyperpolarized gas magnetic resonance imaging in chronic obstructive pulmonary disease using computational simulations with realistic alveolar geometry. Philos Trans A Math Phys Eng Sci 2009;367:2347–2369. [PubMed: 19414459]
81. Washko GR. The role and potential of imaging in COPD. Med Clin N Am 2012;96:729–743. [PubMed: 22793941]
82. Saam BT, Yablonskiy DA, Kodibagkar VD, Leawoods JC, Gierada DS, Cooper JD, Lefrak SS, Conradi MS. MR imaging of diffusion of (3)He gas in healthy and diseased lungs. Magn Reson Med 2000;44:174–179. [PubMed: 10918314]

83. Salerno M, de Lange EE, Altes TA, Truwit JD, Brookeman JR, Mugler JP, III. Emphysema: hyperpolarized helium 3 diffusion MR imaging of the lungs compared with spirometric indexes–initial experience. Radiology 2002;222:252–260. [PubMed: 11756734]
84. Yablonskiy DA, Sukstanskii AL, Leawoods JC, Gierada DS, Bretthorst GL, Lefrak SS, Cooper JD, Conradi MS. Quantitative in vivo assessment of lung microstructure at the alveolar level with hyperpolarized 3He diffusion MRI. Proc Natl Acad Sci USA 2002;99:3111–3116. [PubMed: 11867733]
85. Gao JH, Lemen L, Xiong J, Patyal B, Fox PT. Magnetization and diffusion effects in NMR imaging of hyperpolarized substances. Magn Reson Med 1997;37:153–158. [PubMed: 8978645]
86. Chen XJ, Moller HE, Chawla MS, Cofer GP, Driehuys B, Hedlund LW, Johnson GA. Spatially resolved measurements of hyperpolarized gas properties in the lung in vivo. Part I: diffusion coefficient. Magn Reson Med 1999;42:721–728. [PubMed: 10502761]
87. Chen XJ, Hedlund LW, Moller HE, Chawla MS, Maronpot RR, Johnson GA. Detection of emphysema in rat lungs by using magnetic resonance measurements of 3He diffusion. Proc Natl Acad Sci USA 2000;97:11478–11481. [PubMed: 11027348]
88. Salerno M, Brookeman JR, Mugler JP, III. Time-dependent hyperpolarized 3He diffusion MR imaging: initial experience in healthy and emphysematous lungs. Galsgow; Scotland, UK, 2001 pp 950.
89. Eberle B, Markstaller K, Schreiber WG, Kauczor HU. Hyperpolarised gases in magnetic resonance: a new tool for functional imaging of the lung. Swiss Med Wkly 2001;131:503–509. [PubMed: 11727668]
90. Peces-Barba G, Ruiz-Cabello J, Cremillieux Y, Rodriguez I, Dupuich D, Callot V, Ortega M, Rubio Arbo ML, Cortijo M, Gonzalez-Mangado N. Helium-3 MRI diffusion coefficient: correlation to morphometry in a model of mild emphysema. Eur Respir J 2003;22:14–19. [PubMed: 12882445]
91. Bidinosti CP, Choukeife J, Nacher PJ, Tastevin G. In vivo NMR of hyperpolarized 3He in the human lung at very low magnetic fields. J Magn Reson 2003;162:122–132. [PubMed: 12762989]
92. Salerno M, Altes TA, Brookeman JR, de Lange EE, Mugler JP, III. Rapid hyperpolarized 3He diffusion MRI of healthy and emphysematous human lungs using an optimized interleaved-spiral pulse sequence. J Magn Reson Imaging 2003;17:581–588. [PubMed: 12720268]
93. Fichele S, Paley MN, Woodhouse N, Griffiths PD, van Beek EJ, Wild JM. Investigating 3He diffusion NMR in the lungs using finite difference simulations and in vivo PGSE experiments. J Magn Reson 2004;167:1–11. [PubMed: 14987592]
94. Stavngaard T, Sogaard LV, Mortensen J, Hanson LG, Schmiedeskamp J, Berthelsen AK, Dirksen A. Hyperpolarized 3He MRI and 81mKr SPECT in chronic obstructive pulmonary disease. Eur J Nucl Med Mol Imaging 2005;32:448–457. [PubMed: 15821964]
95. Morbach AE, Gast KK, Schmiedeskamp J, Dahmen A, Herweling A, Heussel CP, Kauczor HU, Schreiber WG. Diffusion-weighted MRI of the lung with hyperpolarized helium-3: a study of reproducibility. J Magn Reson Imaging 2005;21:765–774. [PubMed: 15906344]
96. Fain SB, Altes TA, Panth SR, et al. Detection of age-dependent changes in healthy adult lungs with diffusion-weighted 3He MRI. Acad Radiol 2005;12:1385–1393. [PubMed: 16253850]
97. Swift AJ, Wild JM, Fichele S, Woodhouse N, Fleming S, Waterhouse J, Lawson RA, Paley MN, Van Beek EJ. Emphysematous changes and normal variation in smokers and COPD patients using diffusion 3He MRI. Eur J Radiol 2005;54:352–358. [PubMed: 15899335]
98. Altes TA, Mata J, de Lange EE, Brookeman JR, Mugler JP. Assessment of lung development using hyperpolarized helium-3 diffusion MR imaging. Journal of Magnetic Resonance Imaging 2006;24:1277–1283. [PubMed: 17096396]
99. Trampel R, Jensen JH, Lee RF, Kamenetskiy I, McGuinness G, Johnson G. Diffusional kurtosis imaging in the lung using hyperpolarized 3He. Magn Reson Med 2006;56:733–737. [PubMed: 16958076]
100. Morbach AE, Gast KK, Schmiedeskamp J, et al. [Microstructure of the lung: diffusion measurement of hyperpolarized 3Helium]. Z Med Phys 2006;16:114–122. [PubMed: 16875024]
101. Tanoli TS, Woods JC, Conradi MS, Bae KT, Gierada DS, Hogg JC, Cooper JD, Yablonskiy DA. In vivo lung morphometry with hyperpolarized 3He diffusion MRI in canines with induced

emphysema: disease progression and comparison with computed tomography. J Appl Physiol 2007;102:477–484. [PubMed: 16873601]

102. Mata JF, Altes TA, Cai J, et al. Evaluation of emphysema severity and progression in a rabbit model: comparison of hyperpolarized 3He and 129Xe diffusion MRI with lung morphometry. J Appl Physiol 2007;102:1273–1280. [PubMed: 17110518]
103. Bink A, Hanisch G, Karg A, Vogel A, Katsaros K, Mayer E, Gast KK, Kauczor HU. Clinical aspects of the apparent diffusion coefficient in He-3 MRI: results in healthy volunteers and patients after lung transplantation. J Magn Reson Imaging 2007;25:1152–1158. [PubMed: 17520719]
104. Quirk JD, Lutey BA, Gierada DS, Woods JC, Senior RM, Lefrak SS, Sukstanskii AL, Conradi MS, Yablonskiy DA. In vivo detection of acinar microstructural changes in early emphysema with 3He lung morphometry. Radiology 2011;260:866–874. [PubMed: 21734160]
105. Diaz S, Casselbrant I, Piitulainen E, Magnusson P, Peterson B, Pickering E, Tuthill T, Ekberg O, Akeson P. Progression of emphysema in a 12-month hyperpolarized He-3-MRI study: lacunarity analysis provided a more sensitive measure than standard ADC analysis. Acad Radiol 2009;16:700–707. [PubMed: 19362025]
106. Diaz S, Casselbrant I, Piitulainen E, Magnusson P, Peterson B, Wollmer P, Leander P, Ekberg O, Akeson P. Validity of apparent diffusion coefficient hyperpolarized 3He-MRI using MSCT and pulmonary function tests as references. Eur J Radiol 2009;71:257–263. [PubMed: 18514455]
107. Diaz S, Casselbrant I, Piitulainen E, Pettersson G, Magnusson P, Peterson B, Wollmer P, Leander P, Ekberg O, Akeson P. Hyperpolarized He-3 apparent diffusion coefficient MRI of the lung: Reproducibility and volume dependency in healthy volunteers and patients with emphysema. J Magn Reson Imaging 2008;27:763–770. [PubMed: 18344208]
108. Evans A, McCormack D, Ouriadov A, Etemad-Rezai R, Santyr G, Parraga G. Anatomical distribution of 3He apparent diffusion coefficients in severe chronic obstructive pulmonary disease. J Magn Reson Imaging 2007;26:1537–1547. [PubMed: 17968961]
109. Parraga G, Ouriadov A, Evans A, McKay S, Lam WW, Fenster A, Etemad-Rezai R, McCormack D, Santyr G. Hyperpolarized 3He ventilation defects and apparent diffusion coefficients in chronic obstructive pulmonary disease: preliminary results at 3.0 Tesla. Invest Radiol 2007;42:384–391. [PubMed: 17507809]
110. Mathew L, Evans A, Ouriadov A, Etemad-Rezai R, Fogel R, Santyr G, McCormack DG, Parraga G. Hyperpolarized He-3 magnetic resonance imaging of chronic obstructive pulmonary disease: Reproducibility at 3.0 tesla. Acad Radiol 2008;15:1298–1311. [PubMed: 18790402]
111. Kirby M, Heydarian M, Wheatley A, McCormack DG, Parraga G. Evaluating bronchodilator effects in chronic obstructive pulmonary disease using diffusion-weighted hyperpolarized helium-3 magnetic resonance imaging. J Appl Physiol 2012;112:651–657. [PubMed: 22162521]
112. Stejskal EO. Use of Spin Echoes in a Pulsed Magnetic-Field Gradient to Study Anisotropic, Restricted Diffusion and Flow. Jour Chem Phys 1965;43:3597–3603.
113. Deppe MH, Parra-Robles J, Ajraoui S, Parnell SR, Clemence M, Schulte RF, Wild JM. Susceptibility effects in hyperpolarized (3)He lung MRI at 1.5T and 3T. J Magn Reson Imaging 2009;30:418–423. [PubMed: 19629971]
114. Xu X, Norquay G, Parnell SR, Deppe MH, Ajraoui S, Hashoian R, Marshall H, Griffiths PD, Parra-Robles J, Wild JM. Hyperpolarized 129Xe gas lung MRI-SNR and T2* comparisons at 1.5 T and 3 T. Magn Reson Med 2012;68:1900–1904. [PubMed: 22294386]
115. Owers-Bradley JR, Fichele S, Bennattayalah A, McGloin CJ, Bowtell RW, Morgan PS, Moody AR. MR tagging of human lungs using hyperpolarized 3He gas. J Magn Reson Imaging 2003;17:142–146. [PubMed: 12500284]
116. Woods JC, Yablonskiy DA, Chino K, Tanoli TS, Cooper JD, Conradi MS. Magnetization tagging decay to measure long-range (3)He diffusion in healthy and emphysematous canine lungs. Magn Reson Med 2004;51:1002–1008. [PubMed: 15122683]
117. Woods JC, Yablonskiy DA, Choong CK, Chino K, Pierce JA, Hogg JC, Bentley J, Cooper JD, Conradi MS, Macklem PT. Long-range diffusion of hyperpolarized 3He in explanted normal and emphysematous human lungs via magnetization tagging. J Appl Physiol 2005;99:1992–1997. [PubMed: 16024528]

118. Conradi MS, Yablonskiy DA, Woods JC, Gierada DS, Bartel SE, Haywood SE, Menard C. The role of collateral paths in long-range diffusion of (3)He in lungs. Acad Radiol 2008;15:675–682. [PubMed: 18486004]
119. Bartel SE, Haywood SE, Woods JC, Chang YV, Menard C, Yablonskiy DA, Gierada DS, Conradi MS. Role of collateral paths in longrange diffusion in lungs. J Appl Physiol 2008;104:1495–1503. [PubMed: 18292298]
120. Wang C, Altes TA, Mugler JP, III, Miller GW, Ruppert K, Mata JF, Cates GD, Jr, Borish L, de Lange EE Assessment of the lung microstructure in patients with asthma using hyperpolarized 3He diffusion MRI at two time scales: comparison with healthy subjects and patients with COPD. J Magn Reson Imaging 2008;28:80–88. [PubMed: 18581381]
121. Basser PJ, Mattiello J, LeBihan D. MR diffusion tensor spectroscopy and imaging. Biophys J 1994;66:259–267. [PubMed: 8130344]
122. West JB. Pulmonary pathophysiology. Baltimore, MD: Williams and Wilkins; 1992 pp 1–54.
123. Gierada DS, Woods JC, Bierhals AJ, et al. Effects of diffusion time on short-range hyperpolarized (3)He diffusivity measurements in emphysema. J Magn Reson Imaging 2009;30:801–808. [PubMed: 19787725]
124. Woods JC, Choong CK, Yablonskiy DA, Bentley J, Wong J, Pierce JA, Cooper JD, Macklem PT, Conradi MS, Hogg JC. Hyperpolarized 3He diffusion MRI and histology in pulmonary emphysema. Magn Reson Med 2006;56:1293–1300. [PubMed: 17058206]
125. Waters B, Owers-Bradley J, Silverman M. Acinar structure in symptom-free adults by Helium-3 magnetic resonance. Am J Respir Crit Care Med 2006;173:847–851. [PubMed: 16439719]
126. Fain SB, Panth SR, Evans MD, Wentland AL, Holmes JH, Korosec FR, O'Brien MJ, Fountaine H, Grist TM. Early emphysematous changes in asymptomatic smokers: detection with 3He MR imaging. Radiology 2006;239:875–883. [PubMed: 16714465]
127. Jacob RE, Laicher G, Minard KR. 3D MRI of non-Gaussian 3He gas diffusion in the rat lung. J Magn Reson 2007;188:357–366. [PubMed: 17827044]
128. Mugler JP, Mata J, Wang HTJ, et al. The apparent diffusion coefficient of 129Xe in the lung: preliminary results. In Proceedings of the 12th Annual Meeting of ISMRM, Kyoto, Japan, 2004, p. 769.
129. Sindile A, Muradian I, Hrovat MI, Johnson DC, Hersman FW, Patz S. Human pulmonary diffusion weighted imaging at 0.2T with hyperpolarized 129Xe. In Proceedings of the 15th Annual Meeting of ISMRM, Berlin, Germany; 2007 p. 1290.
130. Kaushik SS, Cleveland ZI, Cofer GP, et al. Diffusion-weighted hyperpolarized 129Xe MRI in healthy volunteers and subjects with chronic obstructive pulmonary disease. Magn Reson Med 2011;65:1154–1165. [PubMed: 21413080]
131. Kirby M, Svenningsen S, Owrangi A, et al. Hyperpolarized 3He and 129Xe MR imaging in healthy volunteers and patients with chronic obstructive pulmonary disease. Radiology 2012;265:600–610. [PubMed: 22952383]
132. Boudreau M, Xu X, Santyr GE. Measurement of (129) Xe gas apparent diffusion coefficient anisotropy in an elastase-instilled rat model of emphysema. Magn Reson Med 2013;69:211–220. [PubMed: 22378050]
133. Fain SB, Altes TA, O'Halloran R, Sorkness RL, Evans MD, Korosec FR, Grist TM. Comparison of diffusion weighted helium-3 MRI in patients with asthma versus those with COPD. In Proceedings of the 14th Annual Meeting of ISMRM, Seattle, Washington, USA, 2006 p. 1665.
134. Emami K, Rajaei JN, Xin Y, et al. Imaging of airway remodelling in a murine model of bronchial hyper-responsiveness using hyperpolarized gas MRI. In Proceedings of the 19th Annual Meeting of ISMRM, Montreal, Canada, 2011 p. 1894.
135. Bink A, Hanisch G, Karg A, Vogel A, Katsaros K, Mayer E, Gast KK, Kauczor HU. Clinical aspects of the apparent diffusion coefficient in 3He MRI: results in healthy volunteers and patients after lung transplantation. J Magn Reson Imaging 2007;25:1152–1158. [PubMed: 17520719]
136. Stephen MJ, Emami K, Woodburn JM, Chia E, Kadlecek S, Zhu J, Pickup S, Ishii M, Rizi RR, Rossman M. Quantitative assessment of lung ventilation and microstructure in an animal model

of idiopathic pulmonary fibrosis using hyperpolarized gas MRI. Acad Radiol 2010;17:1433–1443. [PubMed: 20934126]

137. Mathew L, Vandyk J, Etemad-Rezai R, Rodrigues G, Parraga G. Hyperpolarized (3)He pulmonary functional magnetic resonance imaging prior to radiation therapy. Med Phys 2012;39:4284–4290. [PubMed: 22830762]
138. Mathew L, Gaede S, Wheatley A, Etemad-Rezai R, Rodrigues GB, Parraga G. Detection of longitudinal lung structural and functional changes after diagnosis of radiation-induced lung injury using hyperpolarized 3He magnetic resonance imaging. Med Phys 2010;37:22–31. [PubMed: 20175462]
139. Ward ER, Hedlund LW, Kurylo WC, Wheeler CT, Cofer GP, Dewhirst MW, Marks LB, Vujaskovic Z. Proton and hyperpolarized helium magnetic resonance imaging of radiation-induced lung injury in rats. Int J Radiat Oncol Biol Phys 2004;58:1562–1569. [PubMed: 15050337]
140. Hegarty E, Ouriadov A, Fox MS, Wong E, Welch ID, Santyr GE. Mapping of 129Xe apparent diffusion coefficient anisotropy in radiation-induced lung injury. In Proceedings of the 20th Annual Meeting of ISMRM, Melbourne, Australia, 2012 p. 3981.
141. Narayanan M, Owers-Bradley J, Beardsmore CS, et al. Alveolarization continues during childhood and adolescence: new evidence from helium-3 magnetic resonance. Am J Respir Crit Care Med 2012;185:186–191. [PubMed: 22071328]
142. Cadman RV, Lemanske RF, Jr, Evans MD, Jackson DJ, Gern JE, Sorkness RL, Fain SB. Pulmonary (3)He magnetic resonance imaging of childhood asthma. J Allergy Clin Immunol 2012;131:369–376. [PubMed: 23246019]
143. Callaghan PT. Principles of nuclear magnetic resonance microscopy.Oxford, NY: Claredon Press; 1991.
144. Sukstanskii AL, Yablonskiy DA. In vivo lung morphometry with hyperpolarized (3)He diffusion MRI: theoretical background. J Magn Reson 2008;190:200–210. [PubMed: 18037313]
145. Sukstanskii AL, Conradi MS, Yablonskiy DA. 3He lung morphometry technique: accuracy analysis and pulse sequence optimization. J Magn Reson 2010;207:234–241. [PubMed: 20937564]
146. Yablonskiy DA, Sukstanskii AL, Woods JC, Gierada DS, Quirk JD, Hogg JC, Cooper JD, Conradi MS. Quantification of lung microstructure with hyperpolarized 3He diffusion MRI. J Appl Physiol 2009;107:1258–1265. [PubMed: 19661452]
147. Sukstanskii AL, Yablonskiy DA. Lung morphometry with hyperpolarized (129) Xe: theoretical background. Magn Reson Med 2011;67:856–866. [PubMed: 21713985]
148. Mair RW, Cory DG, Peled S, Tseng CH, Patz S, Walsworth RL. Pulsed-field-gradient measurements of time-dependent gas diffusion. J Magn Reson 1998;135:478–486. [PubMed: 9878475]
149. Mair RW, Wong GP, Hoffmann D, Hurlimann MD, Patz S, Schwartz LM, Walsworth RL. Probing porous media with gas diffusion MRI. Phys Rev Lett 1999;83:3324–3327. [PubMed: 11543587]
150. Fichele S, Paley MN, Woodhouse N, Griffiths PD, Van Beek EJ, Wild JM. Finite-difference simulations of 3He diffusion in 3D alveolar ducts: comparison with the "cylinder model". Magn Reson Med 2004;52:917–920. [PubMed: 15389957]
151. Kitaoka H, Tamura S, Takaki R. A three-dimensional model of the human pulmonary acinus. J Appl Physiol 2000;88:2260–2268. [PubMed: 10846044]
152. Grebenkov DS. NMR survey of reflected Brownian motion. Rev Mod Phys 2007;79:1077–1137.
153. Verbanck S, Paiva M. Model simulations of gas mixing and ventilation distribution in the human lung. J Appl Physiol 1990;69:2269–2279. [PubMed: 2077025]
154. Verbanck S, Paiva M. Simulation of the apparent diffusion of helium-3 in the human acinus. J Appl Physiol 2007;103:249–254. [PubMed: 17379747]
155. Perez-Sanchez JM, Rodriguez I, Ruiz-Cabello J. Random walk simulation of the MRI apparent diffusion coefficient in a geometrical model of the acinar tree. Biophys J 2009;97:656–664. [PubMed: 19619480]

156. Miller GW, Carl M, Mata JF, Cates GD, Jr, Mugler JP, III. Simulations of short-time diffusivity in lung airspaces and implications for S/V measurements using hyperpolarized-gas MRI. IEEE Trans Med Imaging 2007;26:1456–1463. [PubMed: 18041261]

157. Tsuda A, Filipovic N, Haberthur D, Dickie R, Matsui Y, Stampanoni M, Schittny JC. Finite element 3D reconstruction of the pulmonary acinus imaged by synchrotron X-ray tomography. J Appl Physiol 2008;105:964–976. [PubMed: 18583378]

158. Burrowes KS, Tawhai MH, Hunter PJ. Modeling RBC and neutrophil distribution through an anatomically based pulmonary capillary network. Ann Biomed Eng 2004;32:585–595. [PubMed: 15117032]

159. Horsfield K Pulmonary airways and blood vessels considered as confluent trees In: Crystal RG, West JB, Barnes PJ, Cherniack NS, editors. The lung: scientific foundations. New York: Raven Press, Ltd; 1991 p. 721–727.

160. West JB. Respiratory physiology - the essentials. Baltimor, MD: Williams and Wilkins; 1995.

161. Phalen RF, Oldham MJ. Tracheobronchial airway structure as revealed by casting techniques. Am Rev Respir Dis 1983;128(Pt 2):S1–S4.

162. Plopper CG, Mariassy AT, Lollini LO. Structure as revealed by airway dissection. A comparison of mammalian lungs. Am Rev Respir Dis 1983;128(Pt 2):S4–S7. [PubMed: 6881706]

163. Bastacky J, Hayes TL, von Schmidt B. Lung structure as revealed by microdissection. Positional morphology of human lung. Am Rev Respir Dis 1983;128(Pt 2):S7–S13. [PubMed: 6881714]

164. Hartroft WS. Microscopic diagnosis of pulmonary emphysema. Am J Pathol 1945;21:889–903. [PubMed: 19970843]

165. Paiva M Gaseous diffusion in an alveolar duct simulated by a digital computer. Comput Biomed Res 1974;7:533–543. [PubMed: 4457269]

166. Osmanagic E, Sukstanskii AL, Quirk JD, Woods JC, Pierce RA, Conradi MS, Weibel ER, Yablonskiy DA. Quantitative assessment of lung microstructure in healthy mice using an MR-based 3He lung morphometry technique. J Appl Physiol 2011;109:1592–1599.

167. Wang W, Nguyen NM, Yablonskiy DA, Sukstanskii AL, Osmanagic E, Atkinson JJ, Conradi MS, Woods JC. Imaging lung microstructure in mice with hyperpolarized 3He diffusion MRI. Magn Reson Med 2011;65:620–626. [PubMed: 21337400]

168. Xu X, Boudreau M, Ouriadov A, Santyr GE. Mapping of (3) He apparent diffusion coefficient anisotropy at sub-millisecond diffusion times in an elastase-instilled rat model of emphysema. Magn Reson Med 2012;67:1146–1153. [PubMed: 22135238]

169. Ruppert K, Quirk JD, Mugler JP, Altes TA, Wang C, Miller GW, Ruset IC, Mata J, Hersman FW, Yablonskiy DA. Lung morphometry using hyperpolarized xenon-129: preliminary experience. In Proceedings of the 20th Annual Meeting of ISMRM, Melbourne, Australia, 2012 p. 1352.

170. Ouriadov A, Farag A, Kirby M, McCormack D, Parraga G, Santyr G. Hyperpolarized 129 Xe apparent diffusion coefficient anisotropy in chronic obstructive pulmonary disease. In Proceedings of the 20th Annual Meeting of ISMRM, Melbourne, Australia p. 3988.

171. Stepisnik J Validity limits of Gaussian approximation in cumulant expansion for diffusion attenuation of spin echo. Phys B 1999;270:110–117.

172. Jensen JH, Helpern JA, Ramani A, Lu H, Kaczynski K. Diffusional kurtosis imaging: the quantification of non-gaussian water diffusion by means of magnetic resonance imaging. Magn Reson Med 2005;53:1432–1440. [PubMed: 15906300]

173. Kiselev VG, Il'yasov KA. Is the "biexponential diffusion" biexponential? Magn Reson Med 2007;57:464–469. [PubMed: 17326171]

174. Jensen JH, Helpern JA. MRI quantification of non-Gaussian water diffusion by kurtosis analysis. NMR Biomed 2010;23:698–710. [PubMed: 20632416]

175. Kuhn C, III, Tavassoli F The scanning electron microscopy of elastase-induced emphysema. A comparison with emphysema in man. Lab Invest 1976;34:2–9. [PubMed: 1246121]

176. Morris SM, Stone PJ, Snider GL, Albright JT, Franzblau C. Ultrastructural changes in hamster lung four hours to twenty-four days after exposure to elastase. Anat Rec 1981;201:523–535. [PubMed: 6914132]

177. Finlay GA, O'Donnell MD, O'Connor CM, Hayes JP, FitzGerald MX. Elastin and collagen remodeling in emphysema. A scanning electron microscopy study. Am J Pathol 1996;149:1405–1415. [PubMed: 8863687]

178. Voswinckel R, Motejl V, Fehrenbach A, Wegmann M, Mehling T, Fehrenbach H, Seeger W. Characterisation of post-pneumonectomy lung growth in adult mice. Eur Respir J 2004;24:524–532. [PubMed: 15459128]

179. Soutiere SE, Mitzner W. On defining total lung capacity in the mouse. J Appl Physiol 2004;96:1658–1664. [PubMed: 15075308]

180. Knudsen L, Ochs M, Mackay R, et al. Truncated recombinant human SP-D attenuates emphysema and type II cell changes in SPD deficient mice. Respir Res 2007;8:70. [PubMed: 17915009]

181. Mitzner W, Fallica J, Bishai J. Anisotropic nature of mouse lung parenchyma. Ann Biomed Eng 2008;36:2111–2120. [PubMed: 18633711]

182. Knudsen L, Weibel ER, Gundersen HJ, Weinstein FV, Ochs M. Assessment of air space size characteristics by intercept (chord) measurement: an accurate and efficient stereological approach. J Appl Physiol 2010;108:412–421. [PubMed: 19959763]

183. Lee J, Reddy R, Barsky L, Scholes J, Chen H, Shi W, Driscoll B. Lung alveolar integrity is compromised by telomere shortening in telomerase-null mice. Am J Physiol Lung Cell Mol Physiol 2009;296:L57–70. [PubMed: 18952756]

184. Knust J, Ochs M, Gundersen HJ, Nyengaard JR. Stereological estimates of alveolar number and size and capillary length and surface area in mice lungs. Anat Rec (Hoboken) 2009;292:113–122. [PubMed: 19115381]

185. Kang MJ, Lee CG, Lee JY, Dela Cruz CS, Chen ZJ, Enelow R, Elias JA. Cigarette smoke selectively enhances viral PAMP- and virusinduced pulmonary innate immune and remodeling responses in mice. J Clin Invest 2008;118:2771–2784. [PubMed: 18654661]

186. Butler JP, Loring SH, Patz S, Tsuda A, Yablonskiy DA, Mentzer SJ. Evidence for adult lung growth in humans. New Engl J Med 2012;367:244–247. [PubMed: 22808959]

187. Wang W, Nguyen NM, Guo J, Chang YV, Yablonskiy DA, Pierce RA, Woods JC. Noninvasive in-vivo quantification of compensatory lung growth following pneumonectomy, via 1H and 3He MRI. In Proceedings of the Annual Meeting of ISMRM, Melbourne, Australia, 2012 p. 631.

188. Hajari AJ, Yablonskiy DA, Sukstanskii AL, Quirk JD, Conradi MS, Woods JC. Morphometric changes in the human pulmonary acinus during inflation. J Appl Physiol 2012;112:937–943. [PubMed: 22096115]

189. Sukstanskii AL, Quirk JD, Woods JC, Gierada DS, Lutey BA, Conradi MS, Yablonskiy DA. On the relationship between 3He ADC and lung morphometrical parameters. In Proceedings of the 18th Annual Meeting of the ISMRM, Stockholm, Sweden, 2010 p. 2537.

190. Conradi MS, Yablonskiy DA, Woods JC, Gierada DS, Bartel SE, Haywood SE, Menard C. The role of collateral paths in long-range diffusion of 3He in lungs. Acad Radiol 2008;15:675–682. [PubMed: 18486004]

191. Terry PB, Traystman RJ, Newball HH, Batra G, Menkes HA. Collateral ventilation in man. N Engl J Med 1978;298:10–15. [PubMed: 618444]

192. Macklem PT. Collateral ventilation. New Engl J Med 1978;298:49–50. [PubMed: 618452]

193. Hogg W, Brunton J, Kryger M, Brown R, Macklem P. Gas diffusion across collateral channels. J Appl Physiol 1972;33:568–575. [PubMed: 4635918]

194. Lausberg HF, Chino K, Patterson GA, Meyers BF, Toeniskoetter PD, Cooper JD. Bronchial fenestration improves expiratory flow in emphysematous human lungs. Ann Thorac Surg 2003;75:393–397; [PubMed: 12607646]

195. Fichele S, Paley MN, Woodhouse N, Griffiths PD, van Beek EJ, Wild JM. Measurements and modeling of long range 3He diffusion in the lung using a "slice-washout" method. J Magn Reson 2005;174:28–33. [PubMed: 15809169]

196. Mugler JP, III, Wang C, Miller GW, Cates GD, Jr, Mata JF, Brookeman JR, de Lange EE, Altes TA. Helium-3 diffusion MR imaging of the human lung over multiple time scales. Acad Radiol 2008;15:693–701. [PubMed: 18486006]

197. Feder T US government agencies work to minimize damage due to helium-3 shortfall. Phys Today 2009;62:21–23.

198. Nouls J, Fanarjian M, Hedlund L, Driehuys B. A constant-volume ventilator and gas recapture system for hyperpolarized gas MRI of mouse and rat lungs. Concepts Magn Reson Part B Magn Reson Eng 2011;39:78–88.

199. O'Halloran RL, Holmes JH, Wu YC, Alexander A, Fain SB. Helium-3 MR q-space imaging with radial acquisition and iterative highly constrained back-projection. Magn Reson Med 2010;63:41–50. [PubMed: 19953515]

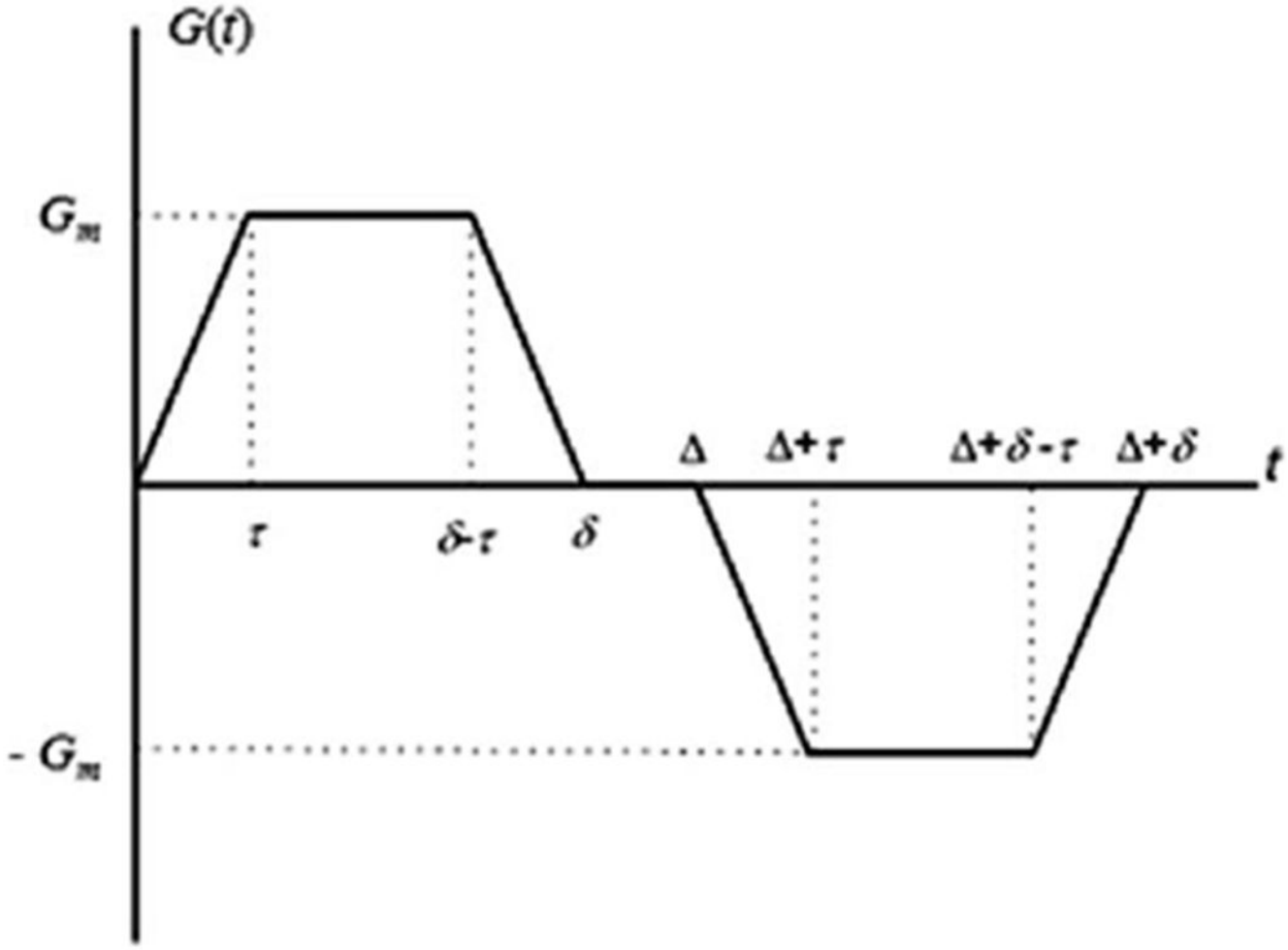

FIG. 1.

Diffusion sensitizing pulse gradient waveform employed in diffusion MRI with hyperpolarized gases at short diffusion times. In this diagram G_m is the gradient lobe amplitude, Δ is the spacing between the leading edges of the positive and negative lobes (the diffusion time), δ is the full duration of each lobe, and τ is a ramp-up and ramp-down time.

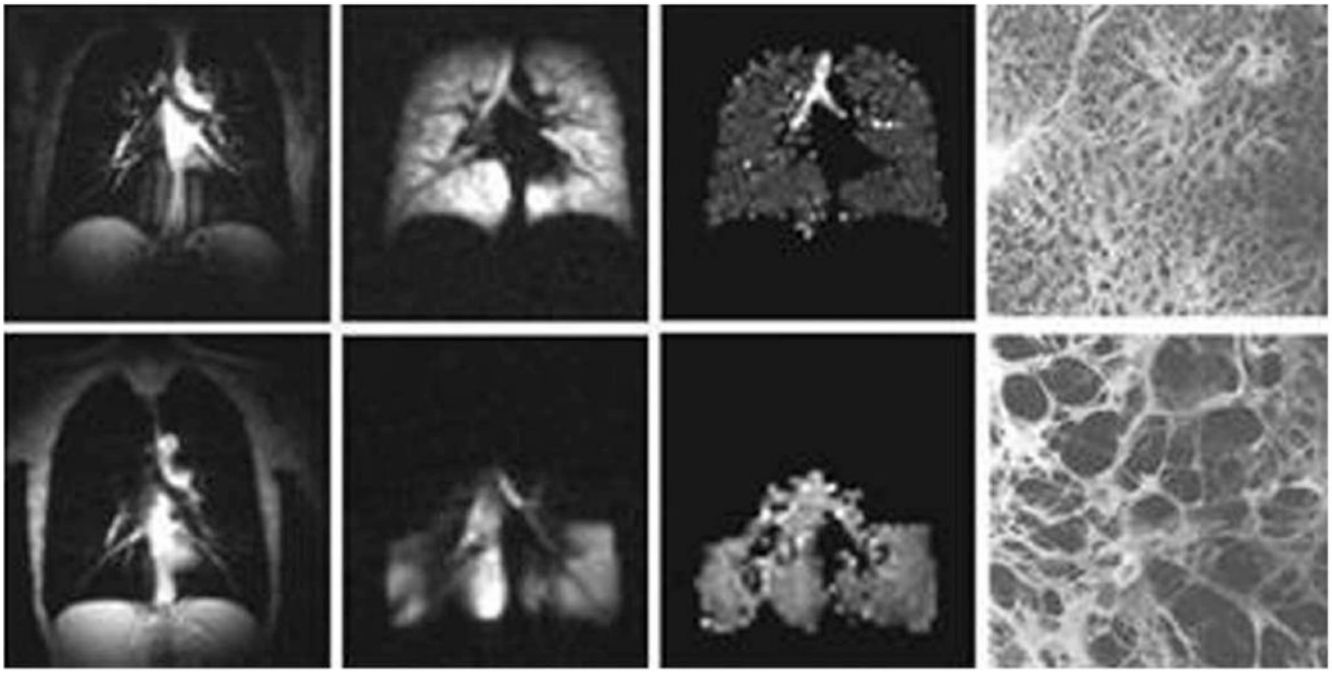

FIG. 2.

Images of normal and emphysematous human lungs. Left to right–proton MRI, ^{3}He ventilation maps, ^{3}He gas ADC maps and histological slices (the latter adapted from Ref. 122); first row–normal lungs, second row–lung with emphysema. ADC in a normal lung is rather homogeneous except for large airways (trachea and its first branches) and is about 0.17 cm^2/s. In the emphysema lung ^{3}He gas penetrates only into ventilated regions (lower portion of the lung in this case) and has an ADC about three times bigger (0.55 cm^2/s) than the ADC in the normal lung.

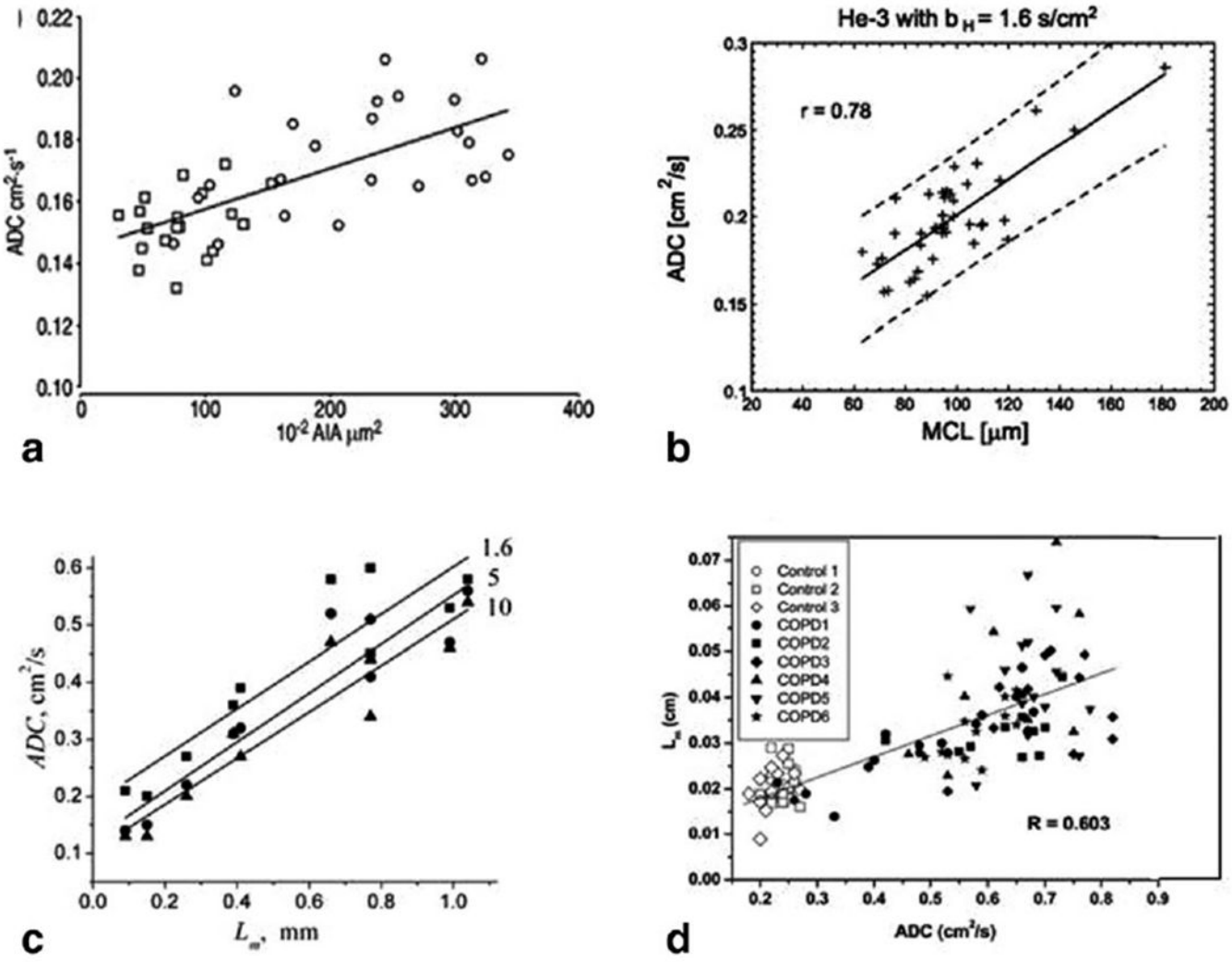

FIG. 3.

Correlation between ADC and (a) mean alveolar internal area (AIA) in rats with elastase induced emphysema (adapted from Ref. 90); (b) mean chord length (MCL) in elastase-induced emphysematous rabbit lungs (adapted from Ref. 102); (c) mean linear intercept L_m in healthy and emphysematous human lungs with data obtained at different diffusion times (in ms, shown by number by the lines) (■) −1.6 ms; (•) −5 ms; (▲) −10 ms) (adapted from Ref. 123); (d) mean linear intercept L_m in healthy human lungs and lungs with severe emphysema (adapted from Ref. 124).

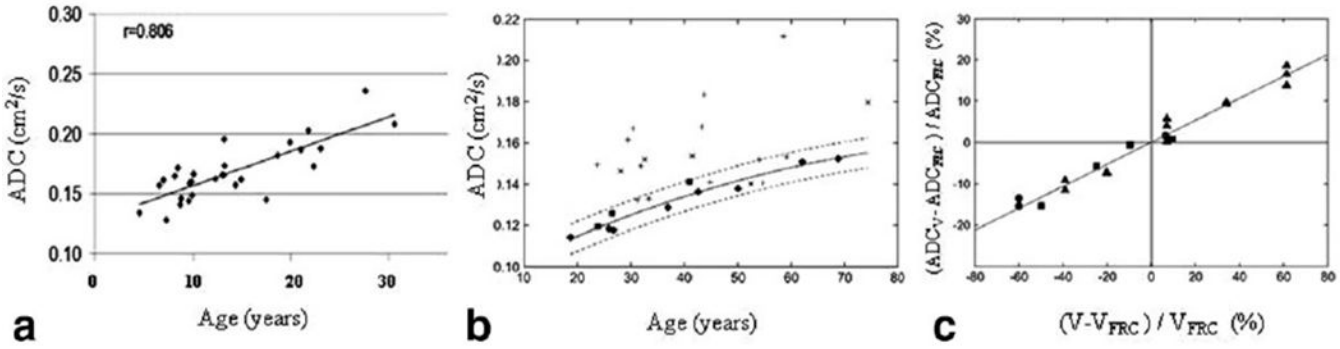

FIG. 4.

ADC dependence on age: (a) (adapted from Ref. 98), (b) (adapted from Ref. 125); and lung inflation (c) (adapted from Ref. 125).

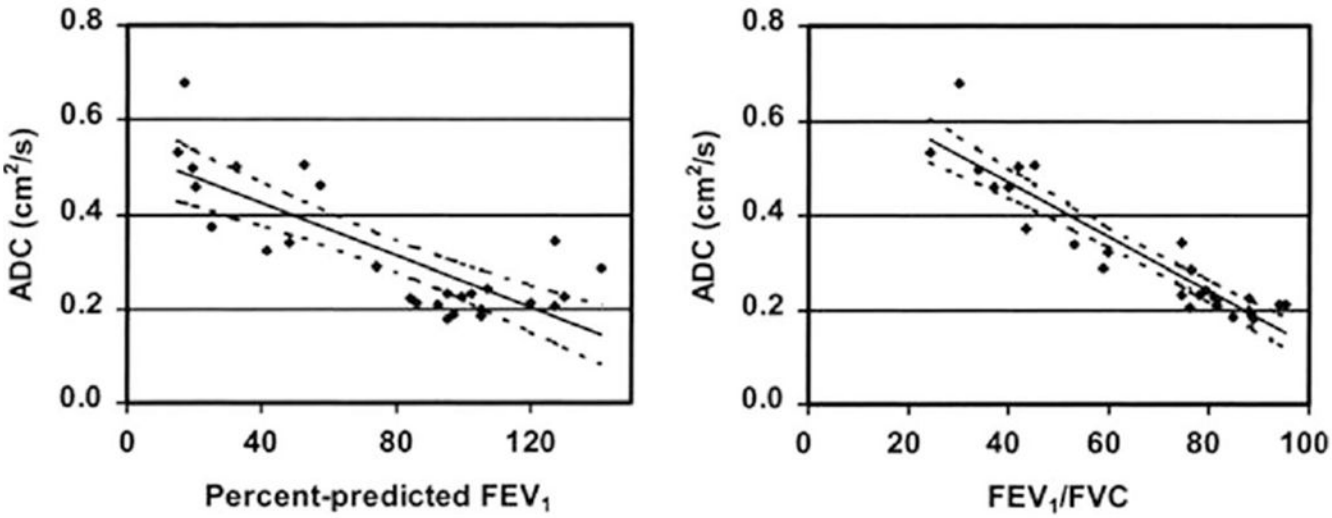

FIG. 5.

Scatter plots depict the relationship between the ADC parameters and spirometric indexes obtained from 16 healthy volunteers and 11 patients with emphysema (adapted from Ref. 83). The 95 % CIs for the regressions are shown as dotted lines. For all subjects, the mean ADCs correlated with the percentage of predicted FEV1 ($r = -0.797$, $P < 0.001$) (left) and FEV1/FVC ($r = -0.930$, $P < 0.001$) (right).

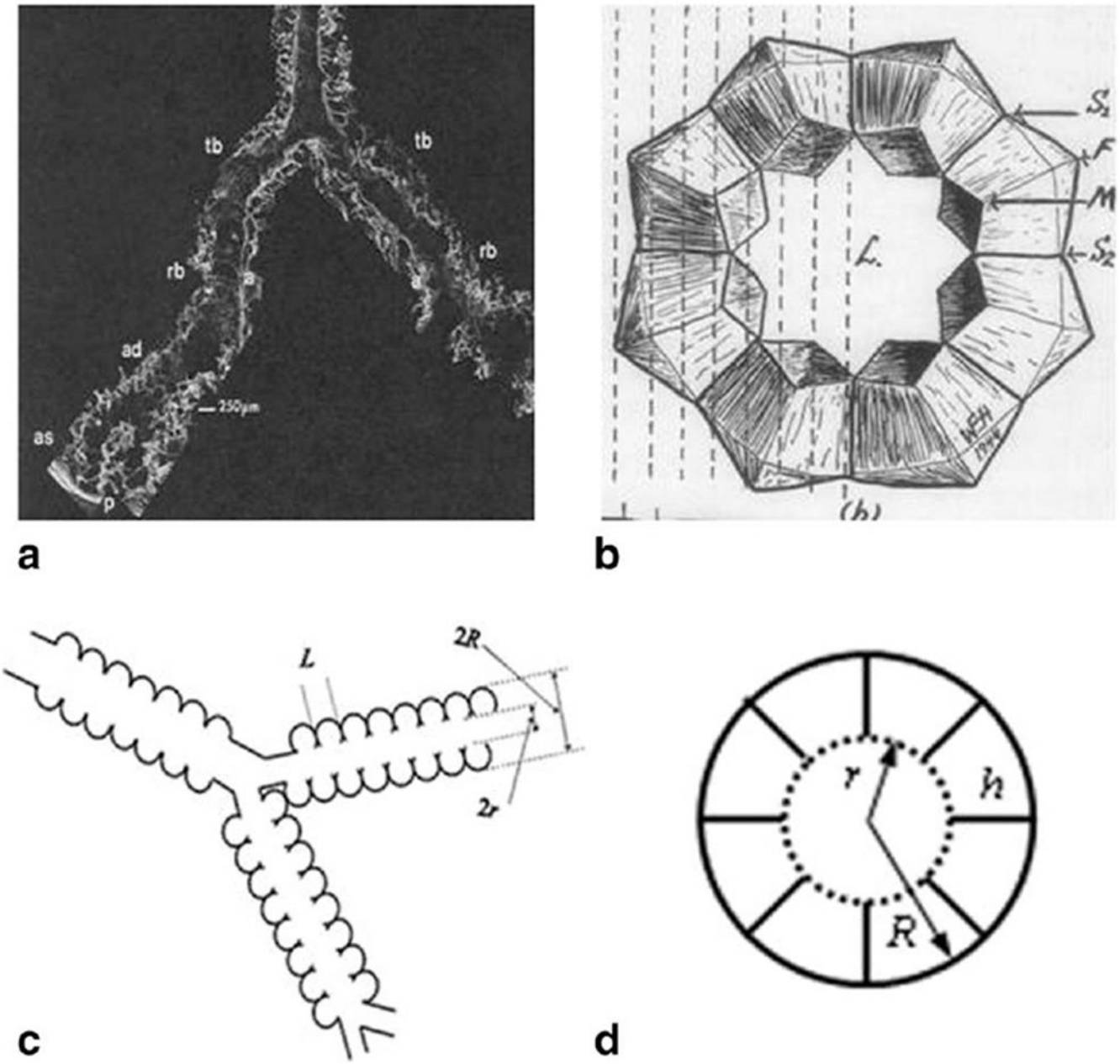

FIG. 6.

a: Distal portion of airways as seen with SEM. Terminal bronchiole (tb), respiratory bronchiole (rb), alveolar duct (ad), alveolar sacs (as), and alveoli (a) are seen in continuity as the airway branches to the pleura (p) (adapted from Ref. 163). b: Schematic drawing of acinar airway cross section representing eight alveoli surrounding the lumen (L) (adapted from Ref. 164). c: Schematic structure of two levels of acinar airways. Open spheres represent alveoli forming an alveolar sleeve around the lumen of each cylindrical airway. d: Cross-section of the acinar airway model (146) with two main parameters: external radius *R* and internal radius *r* (lumen radius) The other parameters, the depth of alveolar sleeve, *h*,

and the alveolar length, L, are: $h = R - r$, $L = 2R\sin(\pi/8) = 0.765\ R$ (8-alveolar model—see discussion below).

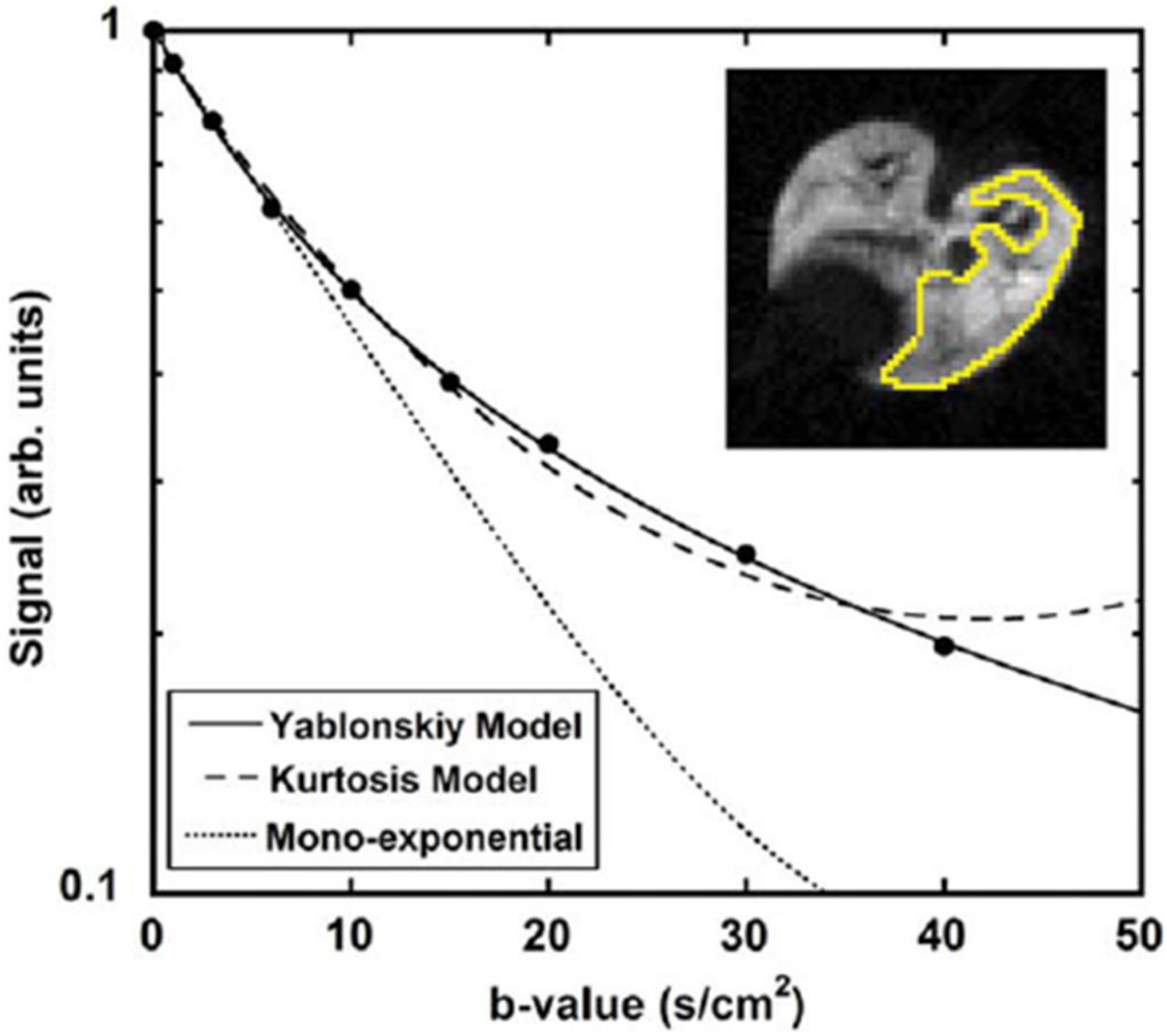

FIG. 7.

^{3}He diffusion MRI signal intensity measured from a rat lung for nine *b*-values in a region of interest (right lung in the inset) (adapted from Ref. 127). The solid line is a fit to the model in Eq. [6], the dashed line is a fit to the kurtosis model, and the dotted line is a fit of the first four data points to a mono-exponential ADC model, imitating the acquisition of only a few low *b*-values.

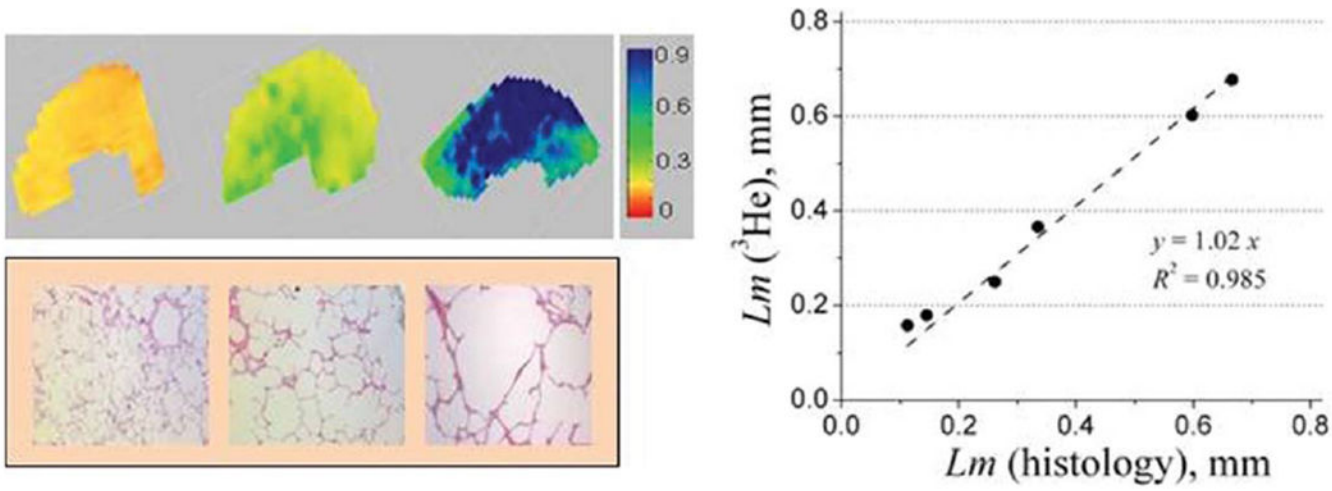

FIG. 8.

Upper row: examples of the L_m (in mm) maps obtained from normal human lung (left) and lungs with different stages of emphysema (mild–middle and severe–right) (adapted from Ref. 146). Lower row: examples of histological slices obtained from the same lungs as above. Right panel: plot of mean linear intercept obtained by means of lung morphometry with hyperpolarized ^{3}He diffusion MRI versus direct measurement. Each point represents one lung. L_m (^{3}He) is median calculated across entire lung; L_m (histology) is median calculated across all lung specimens corresponding to this lung.

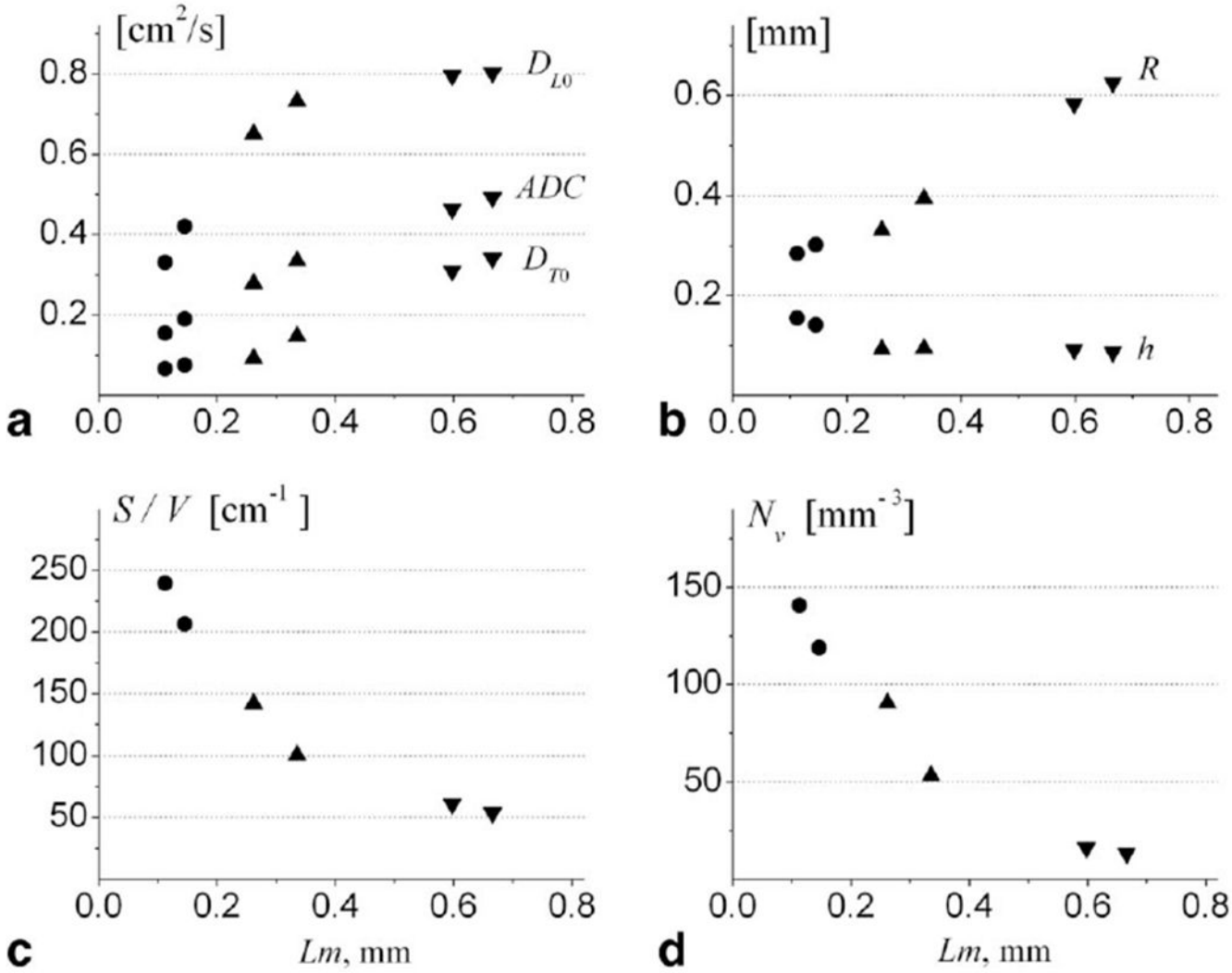

FIG. 9.

Summary of data obtained for six human lung specimens. a: D_{L0}, D_{T0}, and ADC (in cm^2/s); b: R and h (in mm); c: S/V (in cm^{-1}); d: N_V (in mm^{-3}) (adapted from Ref. 146). Markers (•) represent two control healthy lungs, markers (▲)–two lungs with mild emphysema, markers (▼)−two lungs with severe emphysema. Each data point is a median calculated across all imaging voxels for a given lung specimen. Horizontal axis is the mean L_m obtained from direct histological measurements on the same lungs.

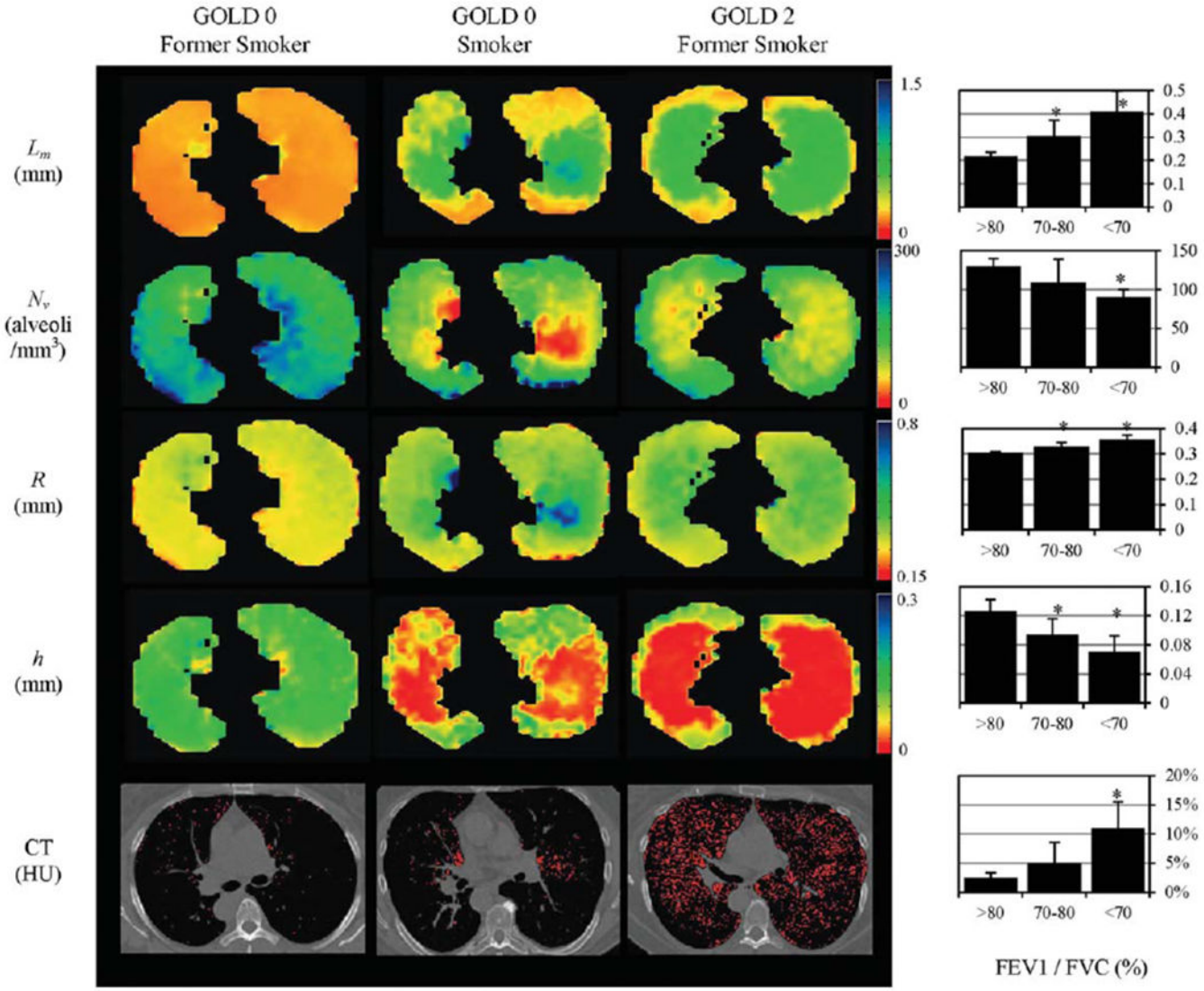

FIG. 10.

Examples of the maps of acinar airways geometric parameters obtained with ^{3}He lung morphometry and CT images for a GOLD 0 former smoker (left, FEV_1 = 93 % predicted, FEV_1/FVC = 80 %), a GOLD 0 smoker (middle, FEV_1 = 94 % predicted, FEV_1/FVC = 71 %), and a GOLD 2 former smoker (right, FEV_1 = 62 % predicted, FEV_1/FVC = 56 %) (adapted from Ref. 104). These images illustrate the heterogeneity of disease across the lungs and the significant increases in R and L_m, and decreases in h and N_v with COPD. Red pixels on the CT images indicate regions of emphysema (attenuation less than −950 HU). Charts on the right summarize results obtained from 30 current and former smokers; they show the increase in (a) mean chord length, (b) $\%EI_{-950}$, and (c) acinar duct radius, and decrease in (d) alveolar depth h with decreasing prebronchodilator FEV_1/FVC by PFT. The FEV_1/FVC <70 % group is statistically significant against all other groups for all measurements shown ($^*P < 0.05$). The FEV_1/FVC 70 to 80 % group is also statistically

significant against all other groups on the ^{3}He lung morphometry measurements (*$P < 0.05$), but not on the CT-based $\%EI_{-950}$. Error bars are standard deviations.

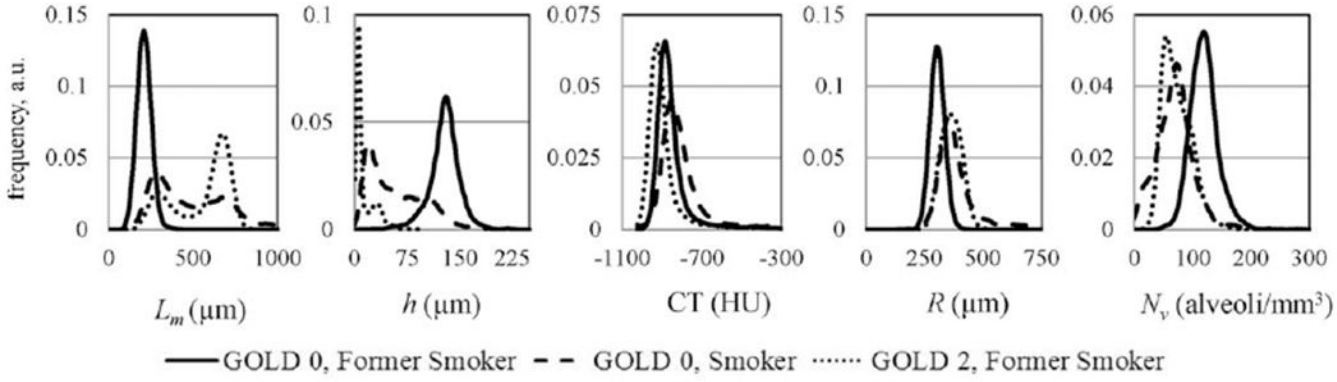

FIG. 11.

Histograms of the lung geometrical parameters and CT images in HU for the subjects in Figure 10.

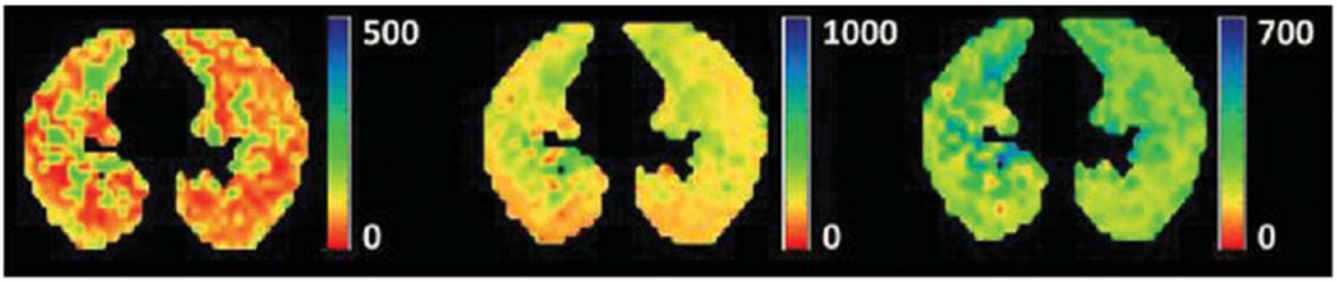

FIG. 12.

Examples of axial maps of alveolar sleeve depth h (left panel) mean linear intercept L_m (middle panel), and acinar-duct radii R (right panel) obtained with ^{129}Xe lung morphometry in a healthy human volunteer at 3 T (adapted from Ref. 169).

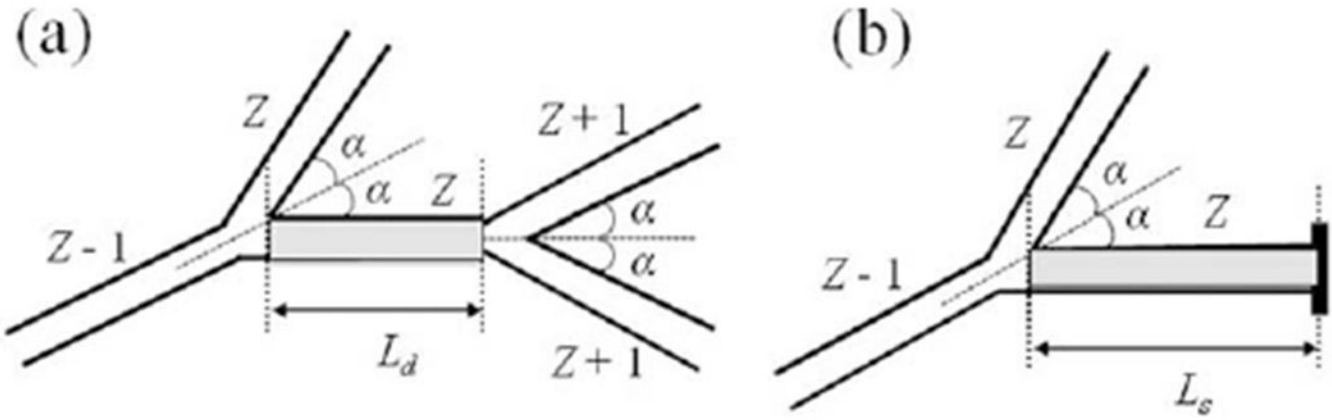

FIG. 13.

Two types of basic airway configurations contributed to MRI signal (adapted from Ref. 145). The internal alveolar structure of the airways is not shown and the aspect ratio is changed for better view of the structures. The first configuration with two nodes (a) corresponds to an alveolar duct of generation Z (shaded airway), surrounded by a "parent" duct of generation ($Z-1$), a "sister" airway of generation Z, and two "daughter" airways of generation ($Z+1$). Symmetrical branching with half-angle $\alpha = 40°$ is assumed. The second configuration with one node (b) corresponds to an alveolar sac of terminal generation Z (shaded airway), surrounded by a "parent" duct of generation ($Z-1$) and a "sister" airway of generation Z.

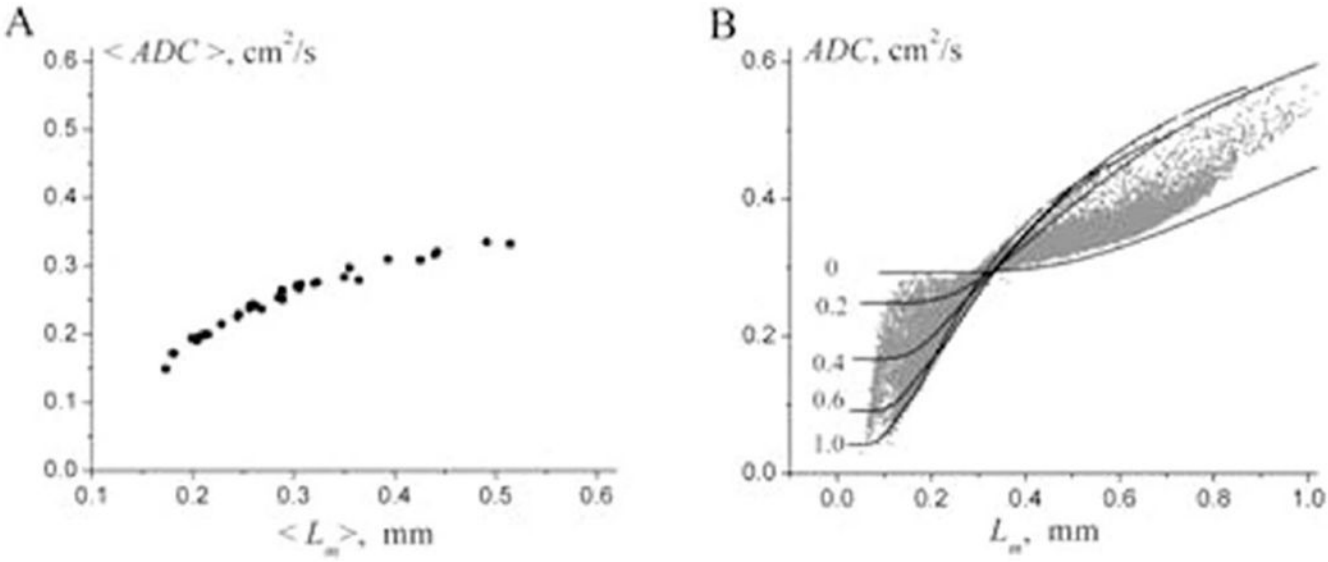

FIG. 14.

ADC versus L_m found for 30 subjects from study (104) (adapted from Ref. 189). a: The average (over each subject) values of the parameters ADC and L_m. b: ADC and L_m calculated on a pixel-by-pixel basis (grey symbols). The lines represent the dependence of ADC as a function of L_m, theoretically calculated at fixed values of the ratio h/R (given by numbers near the lines). Importantly, each value of Lm can be associated with numerous values of ADC, and vice versa.

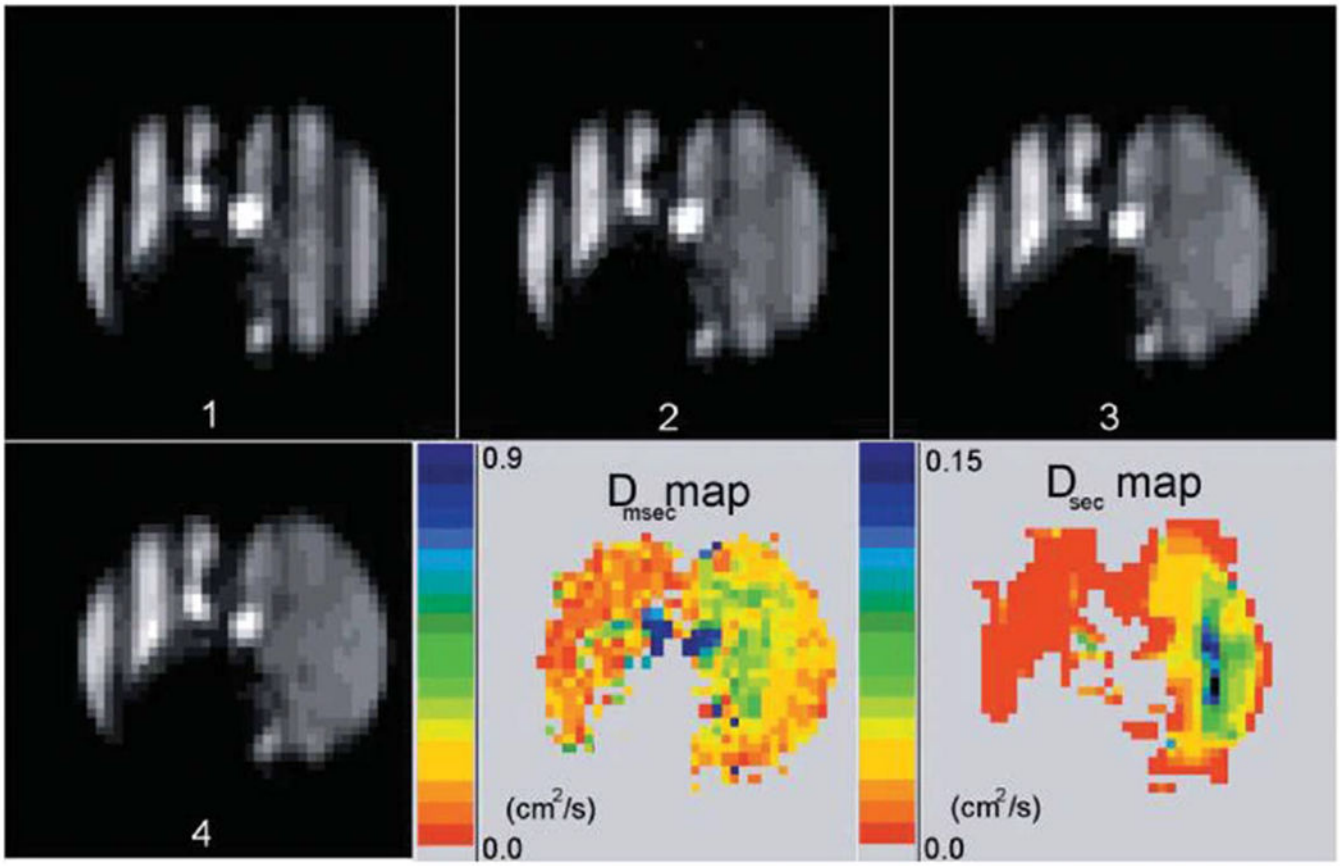

FIG. 15.

Time sequence of tagged images in dog with emphysema in the right lung only (right side of each image) (adapted from Ref. 116). The images have a tagging wavelength of 3 cm and were acquired 0 to 4.1 s after tagging, in equal increments of 1.36 s. The images presented are all from the same slice, out of a total of 10 slices. The LRADC map at lower right is calculated from the decay rate of the fractional modulation on a pixel-by-pixel basis, and shows a substantial difference in LRADC between the two lungs. The fast diffusion is evident from the rapid disappearance of the modulation in the right lung. An ADC map of short-range diffusion is also shown for comparison; note the different scales for LRADC and ADC.

Table 1.

Results Obtained for Lung Acinar Airway Structure Depicted in Figure 13

Input Parameters			Fitting Parameters		
R_0, μm	r_0, μm	$(S/V)_0$, cm^{-1}	R, μm	r, μm	S/V, cm^{-1}
300	140	225	286 (−5%)	135 (−4%)	235 (4%)
300	180	190	296 (−1%)	163 (−9%)	210 (8%)
350	180	183	314 (−10%)	171 (−5%)	196 (7%)
350	220	156	330 (−6%)	199 (−9%)	172 (9%)

The numbers in parenthesis represent the relative difference (%) between the value found from the fitting analysis and the corresponding input value (adapted from (145)).